

AIRCRAFT SAMPLING TO DETERMINE ATMOSPHERIC CONCENTRATIONS AND SIZE DISTRIBUTIONS OF PARTICULATE MATTER AND OTHER POLLUTANTS OVER THE SOUTH COAST AIR BASIN

**FINAL REPORT
CONTRACT No. 96-315**

PREPARED FOR:

**CALIFORNIA AIR RESOURCES BOARD
RESEARCH DIVISION
1001 I STREET
SACRAMENTO, CA 95814**

PREPARED BY:

**J. H. SEINFELD (1)
D. R. COLLINS (1)
H. H. JONSSON (2)
H. LIAO (1)
R. C. FLAGAN (1)
K. J. NOONE (3)
S. V. HERING (4)**

- (1) CALIFORNIA INSTITUTE OF TECHNOLOGY, PASADENA, CA
(2) NAVAL POSTGRADUATE SCHOOL, MONTEREY, CA
(3) STOCKHOLM UNIVERSITY, SWEDEN
(4) AEROSOL DYNAMICS, INC., BERKELEY, CA**

MAY 2000

For more information about the ARB's, Research Division's
research and activities, please visit our Website:

<http://www.arb.ca.gov/research/research.htm>

Disclaimer

The statements and conclusions in this report are those of the contractor and not necessarily those of the California Air Resources Board. The mention of commercial products, their source, or their use in connection with material reported herein is not to be construed as actual or implied endorsement of such products.

Acknowledgments

The authors gratefully acknowledge Prakash Bhave and Glen Cass for providing the back trajectories shown in Figure 3.7. We also thank Yanzeng Zhao for assistance related to the El Monte lidar measurements. This report was submitted in fulfillment of contract 96-315, "Aircraft Sampling to Determine Atmospheric Concentrations and Size Distributions of Particulate Matter and other Pollutants over the South Coast Air Basin", by the California Institute of Technology under the sponsorship of the California Air Resources Board. Work was completed as of January 2000.

Table of Contents

<u>Disclaimer</u>	ii
<u>Acknowledgments</u>	iii
<u>List of Figures</u>	v
<u>List of Tables</u>	vii
<u>Abstract</u>	viii
<u>Executive Summary</u>	ix
Report Body	
<u>1 Introduction</u>	1
<u>2 Materials and Methods</u>	3
<u>2.1 Filter samples</u>	3
<u>2.2 Optical measurements</u>	7
<u>2.3 Size distribution measurements</u>	8
<u>2.4 Optical and mass closure</u>	10
<u>3 Results and Discussion</u>	15
<u>3.1 Three-dimensional aerosol structure</u>	15
<u>3.2 Trajectory studies</u>	23
<u>3.3 Sub-grid variability</u>	25
<u>3.4 Effect of the aerosol on photolysis rates</u>	27
<u>4 Summary and Conclusions</u>	31
<u>References</u>	32
<u>Appendix A: Flight details</u>	35
<u>Appendix B: Filter data</u>	47

List of Figures

Figure 2.2 Schematic of aircraft filter sampling system used. Train A samples were analyzed for trace metals, train B samples for EC/OC, and train C samples for inorganic ions.	5
Figure 2.3 Fine ($D_p < 2.5 \mu\text{m}$) aerosol chemical composition during the seven flights for which samples were collected.	7
Figure 2.4 Comparison of measured size distributions from the DMA, PCASP, and FSSP during two flights that encountered dissimilar aerosol populations.	11
Figure 2.5 Comparison of fine($D_p < 2.5 \mu\text{m}$) aerosol mass determined by summation of individual analyzed species with that determined gravimetrically and that determined through integration of size distributions.	12
Figure 2.6 Closure comparisons between derived and directly measured optical properties. Data presented are from those flights during which filter samples were collected. Comparisons shown include total scattering coefficients measured by the Radiance Research nephelometers at varying relative humidity, hemispherical backscattering at 550 nm measured by the TSI nephelometer, and absorption measured by the PSAP.	14
Figure 3.1 Flight pattern utilized during the first four missions (actual flight track from 8/27 a.m. mission is shown) to study the three-dimensional structure of the aerosol. Arrows indicate the direction(ascending or descending) of each spiral.	15
Figure 3.2 Distribution of PM_{2.5} throughout the Los Angeles basin as sampled during morning and afternoon flights on August 27. The top plots show contours of near-ground level aerosol mass as well as the east-west (E-W) and north-south (N-S) cross sections used in the image plots shown below. Represented in the image plots is PM_{2.5} interpolated from adjacent spirals. The solid grey area at the bottom of each of the image plots represents the approximate ground level.	17
Figure 3.3 The same format as in Figure 3.2 for the aerosol sampled during morning and afternoon flights on August 28.	18
Figure 3.4 Vertical profiles of ambient temperature and aerosol scattering coefficient measured during spirals flown off the coast of Santa Monica on four missions conducted on August 27 and 28.	19
Figure 3.5 (a) Vertical profiles of PM_{2.5} measured during 3000+ m spirals flown over El Monte and Long Beach, and (b) normalized mass size distributions averaged over each of the layers indicated by arrows in (a).	21
Figure 3.6 Vertical profiles representing the mean and standard deviation of a number of extensive and intensive aerosol properties. Data taken during the ten flights during which spirals were flown over El Monte and Riverside, and nine flights with spirals flown over Fullerton were used in the analysis. For the derived ratio of scattering at 80% RH to scattering at 30% RH, only those data below the altitude at which random error began to dominate are shown.	22
Figure 3.7 Flight patterns for missions conducted on September 4 and 5, along with calculated back trajectories for air parcels arriving at Mira Loma and Riverside during the corresponding sampling intervals. Insets show vertical profiles of PM_{2.5} and temperature at spiral locations. The heavy horizontal line in each of the profiles represents the approximate altitude of the circles flown above Diamond Bar, Mira	

<u>Loma, and Riverside. The solid arrows through the flight track represent the direction of maximum aerosol gradient at each of the sampling locations that was used for the analysis presented in Figures 3.8 and 3.9.</u>	24
<u>Figure 3.8 Variation of extensive aerosol properties, intensive aerosol properties, and number size distributions as a function of distance along the direction of maximum gradient indicated in Figure 3.7.....</u>	26
<u>Figure 3.9 The same format as in Figure 3.8 for the aerosol sampled on September 5.....</u>	27
<u>Figure 3.10 Fractional change in five gas-phase photolysis rates calculated to have resulted from the aerosol sampled over El Monte relative to an aerosol-free atmosphere. For each reaction considered, the mean and standard deviation were determined from photolysis rate calculations using measurements made during spirals flown over El Monte on ten flights. Unlike most of the other analyses presented here, altitude is relative to ground level and not sea level.....</u>	28
<u>Figure 3.11 Vertically-resolved fractional change in the NO₂ photolysis rate calculated using data obtained during spirals flown on the morning and afternoon flights of August 28. The east-west cross section indicated in Figure 3.3 was used for presentation of these data.</u>	30

List of Tables

Table 2.1	SCOS97-NARSTO flight summary.....	4
Table 2.2	Measurements made on board the <i>Pelican</i>	4
Table 2.3	Detection limits for species analyzed.....	6

Abstract

As part of the 1997 Southern California Ozone Study-North American Research Strategy for Tropospheric Ozone (SCOS97-NARSTO), a research aircraft was employed during August and September of 1997 to characterize the physical and chemical properties of the aerosol present over the Los Angeles Basin. Aerosol size distributions measured using a differential mobility analyzer and two optical particle counters were combined with filter-based composition measurements to derive a physicochemical description of the aerosol sampled. The accuracy of this description was evaluated through comparison of derived and directly measured aerosol properties including mass, absorption coefficient, hemispherical backscattering coefficient, and total scattering coefficient at two different relative humidities. The sampled aerosol exhibited a complex vertical structure possessing multiple elevated aerosol layers. The most pronounced of these layers were observed to form by injection of aerosol above the ground-level mixed layer along the southern edge of the San Gabriel Mountains. Over multiple inland areas, additional layers were observed at about 2500 m above sea level (asl), while off the coast of Santa Monica, thin but concentrated layers were detected about 500 m asl. In addition to the sharp vertical gradients in aerosol concentration observed, horizontal gradients at multiple locations were found to be sufficient to result in more than 50% variability within a 5 x 5 km computational grid cell commonly used in atmospheric models. Vertically-resolved aerosol measurements made over one location during several flights, as well as over several locations during a morning and afternoon flight on the same day, were used to investigate the temporally- and spatially-resolved impact the aerosol had on gas-phase photolysis rates. These calculations predict that the sampled aerosol enhanced photolysis rates by up to about 5%, although a slight decrease was often observed near ground level.

Executive Summary

Background

Despite substantial improvements, air pollutant concentrations throughout much of Southern California frequently exceed Federal Standards. Only with significant emissions reductions will compliance be achieved. Accomplishing the necessary reductions in an efficient manner requires extensive atmospheric modeling to link specific control scenarios with probable air quality outcomes. The complex terrain and meteorology associated with Southern California, coupled with inherent uncertainties in model input fields, complicates these efforts. Aircraft-based measurements have demonstrated that vertical transport in the Los Angeles area is not consistent with the simple representation of a mixed layer trapped below a temperature inversion. In addition to the poorly characterized variation of species concentrations with altitude, strong horizontal gradients pose a unique problem for models; observed variations within a computational grid cell (typically 5 x 5 km) call into question the assumption that concentrations are uniform inside a grid volume. To date, most aircraft-based studies have focused on ozone and other gas-phase species and have included only limited measures of the aerosol phase. Differing sources, sinks, and controlling processes prevent simple extrapolation of these results to aerosol-phase pollutants, which will likely increase in importance in response to tightening particulate matter standards.

Methods

Between August 27 and September 12, 1997 the Center for Interdisciplinary Remotely-Piloted Aircraft Studies *Pelican* aircraft flew 12 missions over the Los Angeles Basin. To address a number of issues related to aerosol properties and distribution, a range of flight plans were employed. Aerosol composition was determined using three parallel filter samplers. Aerosol size distributions for particles between approximately 10 nm and 20 μm were measured with ~ 1 min time resolution by a differential mobility analyzer and two optical particle counters. Direct measurement of aerosol optical properties was achieved through the use of an absorption photometer and three integrating nephelometers. To test the consistency of the various measures of the aerosol, a range of closure comparisons were performed.

Results

The aerosol present over the Los Angeles Basin exhibits a complex three-dimensional structure. Vertically-resolved data suggest that pronounced elevated layers present over the inland areas were formed through injection of aerosol above the ground-level polluted layer along the Southern edge of the San Gabriel Mountains, followed by advection towards the coast through incorporation into the sea breeze return flow. Additional layers were observed about 500 m asl off the coast of Santa Monica, and approximately 2500 m asl over El Monte and Long Beach. Constant altitude circles flown over Diamond Bar, Mira Loma, and Riverside yielded evidence of gradients in aerosol concentration sufficient to cause over 50% variability within a 5 x 5 km computational grid cell commonly used in atmospheric models. Radiative transfer computations

employing these data suggest that, on average, the aerosol decreased a number of gas-phase photolysis rates in the first 100 m above ground-level, but led to a more pronounced (up to ~5%) increase above that height.

Conclusions

Collectively, the data obtained in this sampling program provide further insight into microphysical processes that govern the size, composition, and spatial and temporal behavior of the Los Angeles aerosol. Coupled with the vast database collected during SCOS97-NARSTO, these data will facilitate development of increasingly powerful atmospheric models.

1 Introduction

Southern California has long struggled to comply with state and federal air quality standards. Faced with a steadily increasing population and tightening ozone and particulate matter standards, further emissions reductions will be necessary. Extensive atmospheric modeling efforts have provided a means for linking specific emission control scenarios with probable air quality outcomes (see, for example, Meng et al., 1997). However, the complex terrain and meteorology associated with Southern California, coupled with inherent uncertainties in model input fields, complicates these efforts. Aircraft-based measurements (Blumenthal et al., 1978; Wakimoto and McElroy, 1986) have demonstrated that vertical transport in the Los Angeles area is not consistent with the simple representation of a mixed layer trapped below a temperature inversion. Recently, three-dimensional meteorological models have provided further insight into mechanisms responsible for formation of distinct pollution layers that exist above the Los Angeles Basin for extended periods of time (Lu and Turco, 1994, 1995). Successful prediction of ground-level concentrations can only be accomplished if the behavior and nature of material aloft are adequately described. In addition to the poorly characterized variation of species concentrations with altitude, strong horizontal gradients pose a unique problem for models; observed variations within a computational grid cell (typically 5 x 5 km) call into question the assumption that concentrations are uniform inside a grid volume. Use of a single measurement within a grid cell to represent the entire cell can lead to uncertainties as high as 25-45%, depending on the species of interest (McNair et al., 1996).

During the summer and fall of 1987, the Southern California Air Quality Study (SCAQS) was undertaken to provide a sufficiently detailed data set to test the capabilities of available meteorological and air quality models. Data from SCAQS, particularly a small number of multi-day episodes, have served as the foundation for most of the modeling work in the years since (Pandis et al., 1992; Harley et al., 1993; Pandis et al., 1993; Jacobson, 1997; Lurmann et al., 1997; Lu et al., 1997; Meng et al., 1998). Ten years after SCAQS, during the summer and fall of 1997, the Southern California Ozone Study-North American Research Strategy for Tropospheric Ozone (SCOS97-NARSTO) was conducted in order to supplement the data set acquired during SCAQS by employing a network of emissions, meteorological, and air quality measurements. The stated goals of SCOS97-NARSTO were:

1. Update and improve the existing aerometric and emission databases and model applications for representing urban-scale ozone episodes in Southern California.
2. Quantify the contributions of ozone generated from emissions in one Southern California air basin to federal and state ozone standard exceedances in neighboring air basins.
3. Apply modeling and data analysis methods to design regional ozone attainment strategies.

To satisfy goal 2, the study covered an extensive region that was roughly bounded by the Channel Islands to the West, the San Joaquin Valley to the North, and the California state border to the East and South. In all, the study encompassed approximately 53,000 square miles,

although a large fraction of the measurements were made within the Los Angeles Basin. SCOS97-NARSTO was conducted between mid-June and mid-October when the highest pollutant concentrations are usually observed in the region. However, during this campaign unusually high sea surface temperatures caused by a significant El Niño event resulted in deeper marine layers and enhanced mixing relative to typical conditions in Southern California. Hence, air pollutant concentrations tended to be somewhat lower during this study than is common for the region.

As its name implies, the Southern California Ozone Study was conducted primarily to improve our understanding of ozone and its gas-phase precursors. A smaller, but still extensive, component of the study focused on understanding the formation and evolution of the atmospheric aerosol. The expanded monitoring network in place for the ozone study facilitated interpretation of aerosol measurements. As part of the aerosol component of SCOS97-NARSTO, a research aircraft was utilized during August and September of 1997 to provide a three-dimensional characterization of the Los Angeles aerosol. This paper presents a description of the measurements obtained by that aircraft during the study period, and an analysis of the impact the aerosol column may have on key gas-phase photolysis rates involved in ozone production.

2 Materials and Methods

Between August 27 and September 12, 1997 the Center for Interdisciplinary Remotely-Piloted Aircraft Studies (CIRPAS) *Pelican* aircraft (Figure 2.1) flew 12 missions over the Los Angeles Basin. The *Pelican* is a Cessna Skymaster that has been modified by replacing the front engine with an extended nose cowling that serves as the primary instrumentation bay. The resulting pusher configuration is ideal for aerosol measurements because it minimizes the disturbance of the atmosphere prior to sampling. Although flight patterns varied, each entailed a combination of ascending and descending spirals, and constant altitude orbits and traverses. A summary of the 12 missions conducted during SCOS97-NARSTO is given in Table 2.1. Optical particle counters were mounted on each of the wings, while the remaining instruments were located inside the aircraft. These latter instruments sampled from two parallel inlets, each of which included a cyclone with a nominal cut size of $2.5\ \mu\text{m}$. Table 2.2 contains a complete list of instruments on board the *Pelican* during SCOS97-NARSTO.



Figure 2.1 CIRPAS *Pelican*

2.1 Filter samples

The chemical composition of the aerosol was probed using the filter system depicted in Figure 2.2. Three parallel sampling trains were utilized; the flow rate of each was set at a nominal rate of $24\ \text{L min}^{-1}$ and continuously recorded. Separate trains were used for analysis of

trace metals, elemental and organic carbon, and inorganic ions. Each sampling train consisted of three identical filter cassettes, allowing sequential exposure of multiple filters through the use of cockpit-activated solenoid valves that were in-line with each of the filter cassettes. During SCOS97-NARSTO, three sets of filter samples were taken during each of the first six flights, with two sets taken on the seventh flight. Filters were unloaded immediately following each flight and remained refrigerated during storage and transport until analysis. Several filter blanks were taken from each sampling train and were used to correct for the samples analyzed.

Table 2.1 SCOS97-NARSTO flight summary.

Flight #	Date	Start time	End time	Primary focus of mission
1	8/27	06:06	10:33	Three-dimensional aerosol distribution
2	8/27	13:03	17:29	“ “
3	8/28	06:08	10:40	“ “
4	8/28	13:00	17:45	“ “
5	9/4	09:50	14:55	Nitrate production and aerosol spatial variability
6	9/5	13:50	18:55	“ “
7	9/6	11:30	14:44	Nitrate production and aerosol vertical variability
8	9/9	06:40	09:36	Detailed vertical profile over multiple locations
9	9/10	08:30	11:52	“ “
10	9/10	14:00	16:55	“ “
11	9/11	10:00	11:39	Near-ground level variation in aerosol properties and concentrations
12	9/12	10:55	14:19	“ “

Table 2.2 Measurements made on board the *Pelican*

Property measured	Instrument	Time resolution
<i>Aerosol measurements</i>		
Inorganic ions, trace metals, EC/OC	Sub-2.5 μm filter samplers	~ 1 h
Particle size (0.01 – 0.5 μm)	DMA	1 min
Particle size (0.15 – 3.0 μm)	PMS PCASP	1 s
Particle size (0.5 – 20 μm)	PMS FSSP	1 s
Light scattering coefficient (3-color)	TSI 3563 humidigraph	1 s
Light scattering / RH relationship	UW Humidigraph (Radiance Research nephelometers)	6 s
<i>Radiation measurements</i>		
Total solar	Eppley pyranometer	1 s
UV	Eppley radiometer	1 s
<i>Meteorological measurements</i>		
Pressure (static and dynamic), temperature, and dew point	Various	1 s

Sampling train A shown in Figure 2.2 used a Teflon filter to collect samples for gravimetric and trace metal analysis. Inductively-coupled plasma mass spectrometry (ICP-MS) was used to quantify Na^+ , Al^{3+} , K^+ , Ni^{2+} , Zn^{2+} , Mg^{2+} , Si^{4+} , Fe^{3+} , and Cu^{2+} for each of the filters. With the exception of Na^+ and Mg^{2+} that were assumed to be associated with sea salt particles, each of the metals was assumed to be present as oxides (Al_2O_3 , SiO_2 , K_2O , Fe_2O_3 , NiO , CuO , and ZnO) for determination of aerosol mass. Uncertainty in total aerosol mass introduced as a result of this assumption is relatively low since the elements analyzed typically constituted only a small fraction of the aerosol mass.

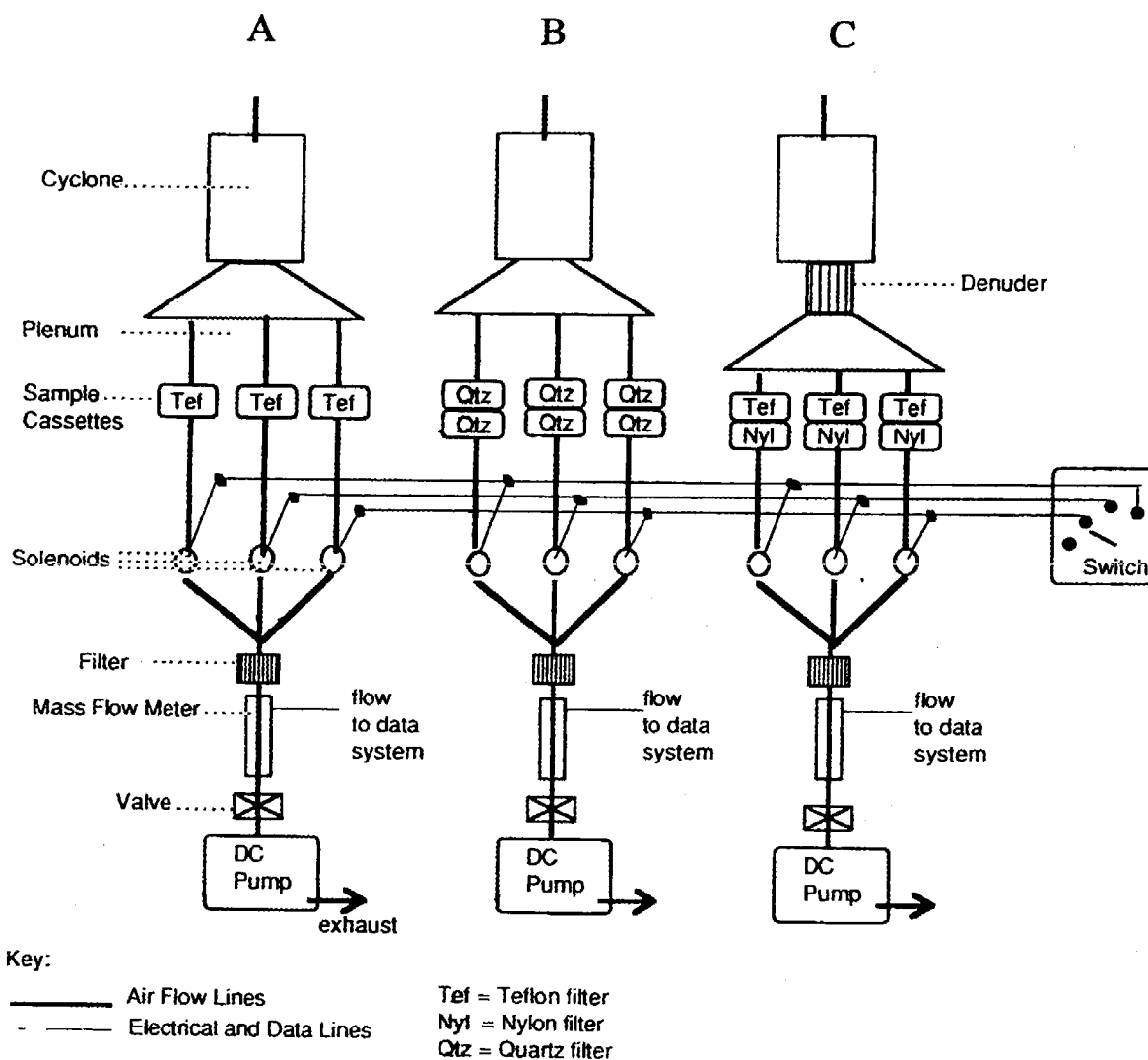


Figure 2.2 Schematic of aircraft filter sampling system used. Train A samples were analyzed for trace metals, train B samples for EC/OC, and train C samples for inorganic ions.

Elemental and organic carbon collected on quartz filters in sampling train B were analyzed through thermal optical reflectance (Chow et al., 1993) by researchers at the Desert Research Institute (DRI). This method continuously assays the blackness of the quartz filter as it is heated to distinguish between organic and elemental carbon. To account for the positive artifact resulting from organic vapor adsorption on the filter, a quartz back-up filter was used, with the corrected organic aerosol mass assumed to be the difference between that measured on the front and back filters. Since oxygen and hydrogen are not detected in this type of analysis, organic carbon loadings were multiplied by 1.4 to estimate total organic aerosol mass (White, 1990).

Train C employed an MgO denuder to remove nitric acid in order to minimize the positive artifact that it might otherwise cause. Downstream of the denuder, a Teflon filter was used to collect aerosol for gravimetric and inorganic ion analysis. Researchers with DRI used ion chromatography to analyze SO_4^{2-} and NO_3^- , while colorimetry was utilized to quantify NH_4^+ . The NO_3^- mass measured on the nylon back-up filter was assumed to be volatilized ammonium nitrate, and was, therefore, used to correct the NH_4^+ , NO_3^- , and total mass measured on the Teflon filter.

Detection limits for each aerosol species analyzed are listed in Table 2.3. The ambient concentration limits are based on the mean sampling period for the filter train (1h 20min) during the study. Aerosol mass for each of the 20 sets of filters analyzed is shown in Figure 2.3. With the exception of the September 4 and 5 flights, filter samples represent the integration of the aerosol present over a relatively wide area and over about 2 km variation in altitude. These spatially-unresolved filter measurements were used to gain a general understanding of the chemical nature of the aerosol and to aid in the analysis of time-resolved size distributions, but were not used to directly assess variations in composition within the study area.

Table 2.3 Detection limits for species analyzed

Species	Analytical limit ($\mu\text{g}/\text{filter}$)	Ambient concentration ($\mu\text{g m}^{-3}$)
SO_4^{2-} , NO_3^- , NH_4^+	0.8	0.4
OC	2	1
EC	0.5	0.3
Fe, Si, K	0.1	0.05
Na	0.01	0.005
Mg, Ni, Cu, Zn, Al	0.001	0.0005
Mass	10	5

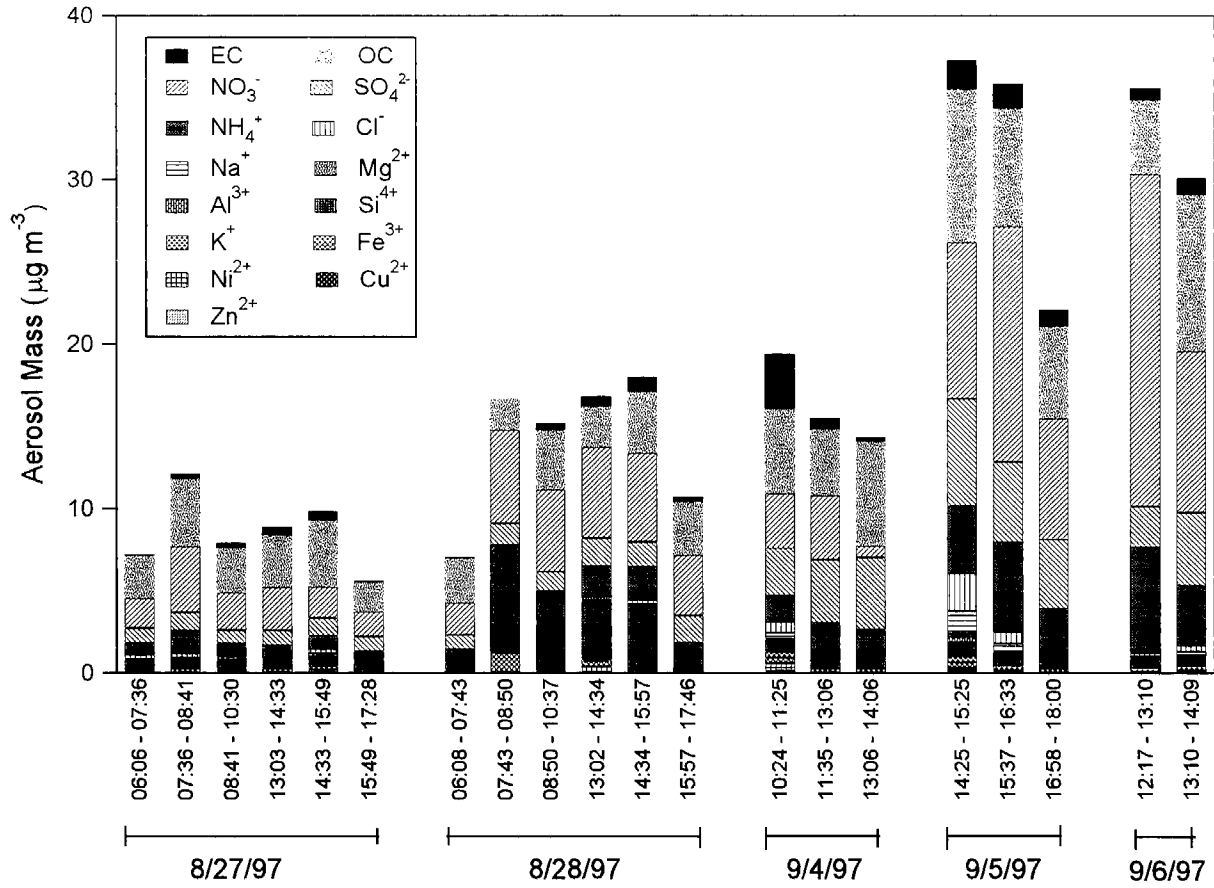


Figure 2.3 Fine ($D_p < 2.5 \mu\text{m}$) aerosol chemical composition during the seven flights for which samples were collected.

2.2 Optical measurements

Three integrating nephelometers and an absorption photometer provided details of the optical and hygroscopic properties of the aerosol sampled during SCOS97-NARSTO. The University of Washington Passive Humidigraph, which consists of two Radiance Research nephelometers operated in parallel at different relative humidities (RH), was used to investigate the relationship between humidity and aerosol light scattering. In general, humidities within the dry and wet nephelometers bracketed the ambient RH. An empirical relationship, first presented by Kasten (1969), can be used to describe the change in scattering associated with varying RH,

$$\sigma_{sp}(RH) = k(1 - RH)^{-\gamma} \quad \text{or} \quad \frac{\sigma_{sp}(RH_1)}{\sigma_{sp}(RH_2)} = \left(\frac{1 - RH_2}{1 - RH_1} \right)^\gamma \quad (2.1)$$

where σ_{sp} is the aerosol scattering coefficient, having units of inverse length, and k and γ are empirically-determined constants. Calculation of γ provides a means of comparing relationships between scattering and RH for aerosol populations sampled at different times since the relative

humidity within each instrument varied during the flight. The third nephelometer used was a TSI 3563 that measures total scattering and hemispherical backscattering at blue (450 nm), green (550 nm), and red (700 nm) wavelengths. Each of the nephelometers was calibrated prior to, or during, the study using gases with known scattering properties.

A Radiance Research Particle Soot Absorption Photometer (PSAP) was used to make time-resolved measurements of the absorption properties of the aerosol. The PSAP continuously records transmittance of light (567 nm) through two regions on a filter, one of which has an aerosol-laden flow passing through it, while the other is used as a reference. The aerosol absorption coefficient, σ_{ap} , is determined from the rate of change of the transmittance ratio between the two regions. PSAP calibration results described by Bond et al. (1999) were used to analyze the data obtained. Their analysis showed that the PSAP is sensitive not only to particle absorption, but also to scattering, and recommended an adjustment related to the concurrently-measured scattering coefficient. Despite the fact that transmittance is normalized to that through a non-exposed part of the filter, variations in transmittance ratio unrelated to increased particle loading are found to occur as a result of pressure variations within the instrument. Clearly, this poses a significant problem for aircraft-based measurements taken during ascending and descending spirals. Only during constant altitude legs did the observed change in transmittance due to particle loading dominate over that caused by pressure variations. As a result, absorption data were available only for limited portions of each flight.

2.3 Size distribution measurements

By integrating measurements from a differential mobility analyzer (DMA) and two optical particle counters (OPCs), aerosol size distributions spanning the range from 10 nm to >20 μm in diameter were determined with 1 min time resolution. A TSI 3071 cylindrical DMA was operated with a TSI 3010 condensation particle counter to size particles with diameters between approximately 10 and 500 nm. Each of the DMA flow rates was actively controlled to minimize fluctuations induced by pressure changes within the instrument. The voltage applied to the DMA was scanned over 45 s, and was automatically adjusted to maximize particle size range, while remaining below the pressure and temperature dependent threshold for electrostatic breakdown. A wing-mounted Particle Measuring Systems (PMS) Passive Cavity Aerosol Spectrometer Probe (PCASP-100X) sized particles ranging from approximately 140 nm to over 3 μm . The PCASP was calibrated prior to SCOS97-NARSTO with polystyrene latex (PSL) particles. Mie theory calculations that accounted for the angular configuration of the light receptor in the PCASP were used to adjust this PSL calibration to that expected for particles of any specified complex index of refraction. Mounted on the wing opposite to the PCASP was a PMS Forward Scattering Spectrometer Probe (FSSP-100). By utilizing an external laser / detector, the FSSP causes only minimal disturbance to large particles and cloud droplets. The 1 Hz measurements of both the PCASP and FSSP were averaged over the ~1 min measurement time of the DMA.

The PCASP and DMA systems both change the relative humidity of the aerosol during the act of sampling, while the FSSP has little effect on this important parameter. To combine these measurements into a coherent description of the sampled aerosol, the ambient particle size distribution must be estimated from the perturbed data. The relative humidities at which the particles are measured within the various instruments differ, so the magnitude of the corrections

also differ. An accurate description of the effect of humidity on particle size requires knowledge of the aerosol composition, mixing state, and deliquescence state. Rarely is this information available, so assumptions must be used in its place. Filter samples taken during the majority of the *Pelican* flights were used to estimate the composition of the sampled aerosol during the respective filter integration interval. For those flights during which no filter samples were taken, the average composition analyzed during the flights with filter measurements was used. Nitrate was assumed to be present as NH_4NO_3 . The molar ratio of ammonium not associated with nitrate to non-sea salt sulfate was used to estimate the degree of neutralization (H_2SO_4 , NH_4HSO_4 , or $(\text{NH}_4)_2\text{SO}_4$) of the sulfate aerosol. The trace metals in the aerosol were assumed to be contained in soil dust particles. Since filter samples were not size-resolved, it was assumed that size-dependent composition and mixing relationships were similar to those described by Zhang et al. (1993) in their analysis of data taken during SCAQS. In general, Zhang et al. (1993) found the distribution of carbon was shifted to slightly smaller particles relative to inorganic species. They also found the fraction of the carbonaceous content of the aerosol that was internally mixed with inorganic species approached unity for particles smaller than approximately 150 nm, but approached zero for particles larger than 500 nm. As expected, their analysis showed that dust particles were largely externally mixed, and had mass distributions that tended toward larger sizes. Though no distinction was made between sea salt and other ions, it is assumed here that sea salt has the same relative size distribution as the dust aerosol. External mixtures of salt particles were assumed so that available single-salt solution thermodynamics data for particle growth / evaporation calculations could be used. Tang (1996) showed that only minor differences exist in overall optical properties of internal and external mixtures of common nitrates and sulfates. Moreover, the similar densities of common nitrates and sulfates limit the uncertainty in the calculated aerosol mass that might be caused by this assumption. The particle size and density dependent penetration efficiency of the cyclone was used in conjunction with the size distributions to calculate a size-resolved aerosol composition for each filter sampling period. As a result, the relative composition determined from filter analyses was the same as that calculated from the physicochemical description of the aerosol.

The ambient relative humidity measured during SCOS97-NARSTO often lay between the crystallization and deliquescence points of the salt species known to be present in the aerosol. Whether the aerosol would be wet or dry under these circumstances depends on the RH history it experienced. Humidity data taken during the flights, coupled with continuous ground-based measurements at five locations in the Los Angeles area, were used to estimate the maximum humidity encountered by the aerosol that was sampled during a given flight. Using these data, a maximum humidity of 55% (deliquescence of NH_4HSO_4) was assumed for the 9/4, 9/5, and 9/10 flights; a maximum of 65% (deliquescence of NH_4HSO_4 and NH_4NO_3) was assumed for the 8/27, 8/28, 9/6, and 9/12 flights; and a maximum of 75% (deliquescence of NH_4HSO_4 , NH_4NO_3 , and sea salt) was assumed for the 9/9 and 9/12 flights. As an estimate of the uncertainty that this assumption might introduce, it was determined that, averaged over all of the flights, $\text{PM}_{2.5}$ (dry aerosol mass $\leq 2.5 \mu\text{m}$ aerodynamic diameter) calculated using the assumption that the maximum humidity encountered was the ambient humidity at that time is only 5.1% greater than that calculated assuming all salts had previously deliquesced.

Combining this chemical description of the aerosol with empirical relationships that describe the density and activity of aqueous solutions of pure salts (Tang and Munkelwitz, 1994;

Tang, 1996) and actual sea salt (Tang et al., 1997) provides a means for adjusting a measured size distribution to a specified relative humidity. Hygroscopic growth was considered only for the salt species, and not for carbon or dust. The assumption that carbonaceous aerosol is non-hygroscopic is known to be incorrect for at least some organic species found in the aerosol phase (Saxena et al., 1995). However, in their interpretation of SCAQS impactor data, Zhang et al. (1993) suggest that externally mixed carbonaceous particles were non-hygroscopic, while carbon internally mixed with salt particles was less hygroscopic than the salt itself. The relatively low humidity encountered throughout the present study, and generally characteristic of the region, further limits uncertainties caused by this assumption. Figure 2.4 shows integrated size distributions from two flights that encountered dissimilar aerosol populations. Data from each of the instruments used have been adjusted to a common relative humidity to permit comparison of the different measurements in overlapping regions. The DMA and PCASP size distributions differ systematically, with the DMA indicating larger particles than the PCASP. The cause of the discrepancy is not known, but it generally had little impact on derived aerosol mass and optical properties. Consistent with the examples shown, size and concentration agreement between the PCASP and FSSP was very good. Lacking definitive evidence of the relative accuracy of the different measurements, individual distributions were simply averaged in overlapping size ranges.

2.4 Optical and mass closure

Although composition and optical measurements afford valuable information about the properties of the sampled aerosol, only an accurate physicochemical description can provide a full range of spatially and temporally resolved aerosol characteristics. In order to test the validity of the size distribution-based physicochemical description of the aerosol, a number of comparisons were performed with the optical and composition measurements. These so-called closure comparisons involve predicting the response of a given instrument to an aerosol population that is described from additional measurements. For the analyses presented here, the aerosol property predictions are based on size distribution and composition measurements. The utility of such comparisons is that they provide confidence in the over-determined set of measurements when closure is achieved, and indicate potential sources of error when it is not.

To estimate aerosol mass collected on the filters during sampling intervals, aerosol size distributions were first adjusted to the relative humidity within the cyclone, which was slightly warmer and, therefore, drier than outside. The density of each aerosol type considered was then calculated and used to determine the appropriate cyclone penetration efficiency *s*-curve. For hygroscopic particles, density was calculated as a function of relative humidity, whereas constant densities of 2.6 g cm⁻³ for dust (Tegen and Fung, 1994), and 2.0 g cm⁻³ and 1.4 g cm⁻³ for elemental and organic carbon, respectively (Larson et al., 1988), were used. The dry aerosol mass (RH ~ 15%) of those particles that passed through the cyclone was then calculated and compared with the mass analyzed on the corresponding filter. A scatter plot showing the relationship between derived and measured aerosol mass is shown in Figure 2.5. Also shown is the gravimetrically-determined aerosol mass for 16 sets of filters for which analysis of the two separate Teflon filters agreed to within two standard deviations, as calculated from repeated measurement of one of the two filters. Although there is some scatter about the 1:1 line, there are no pronounced systematic discrepancies among the three types of mass measurements.

As with aerosol mass calculations, modification of the aerosol size distribution to account for removal in the cyclone is necessary for comparison with the various optical instruments on board. The remaining particles are then adjusted to the relative humidity within each instrument. For those cases in which the relative humidity of the sample flow is reduced below the crystallization point of a given salt, only if the RH in the humidified nephelometer is above the deliquescence point of the salt is it assumed to be hydrated.

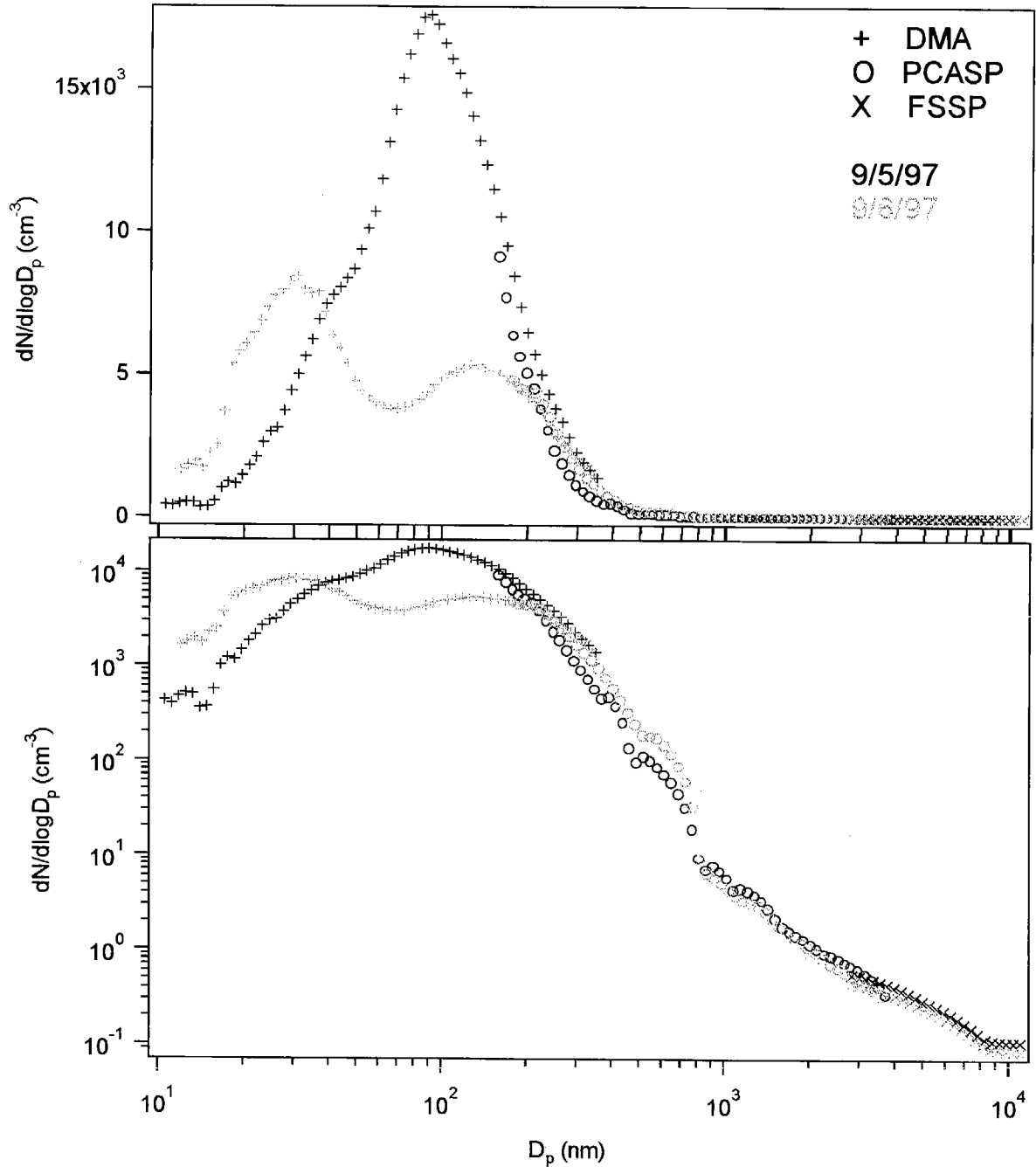


Figure 2.4 Comparison of measured size distributions from the DMA, PCASP, and FSSP during two flights that encountered dissimilar aerosol populations.

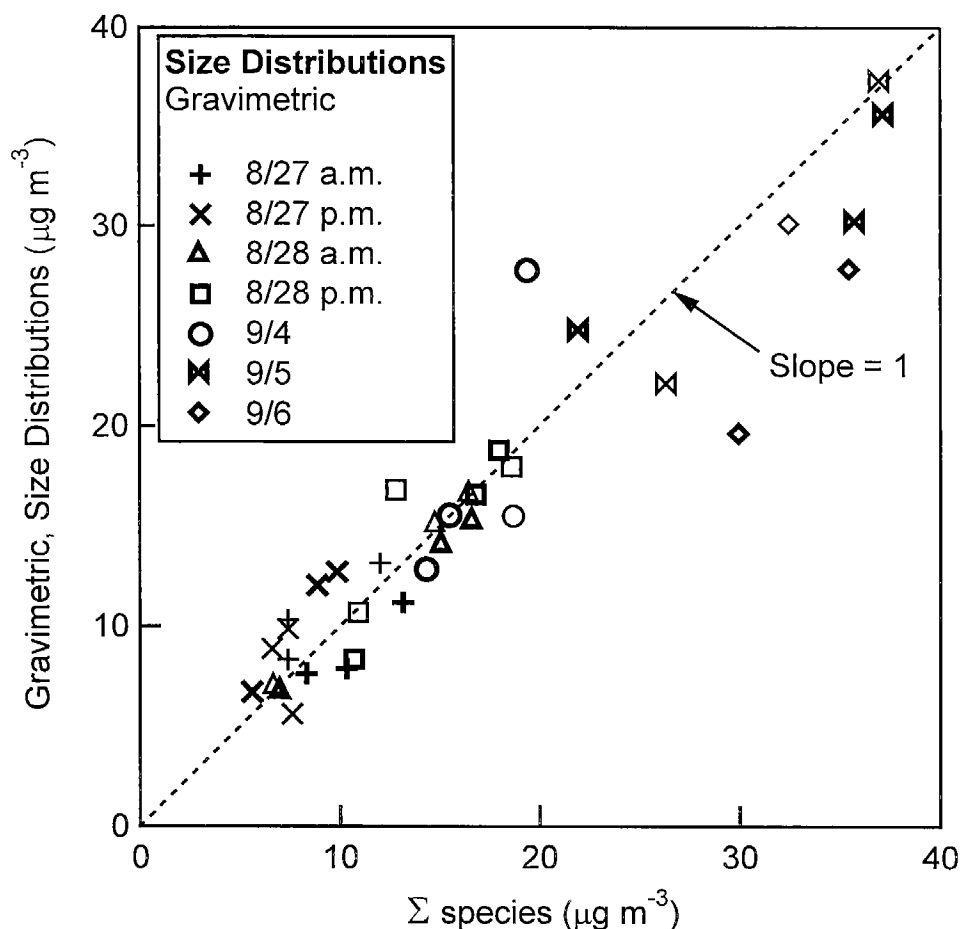


Figure 2.5 Comparison of fine($D_p < 2.5 \mu\text{m}$) aerosol mass determined by summation of individual analyzed species with that determined gravimetrically and that determined through integration of size distributions.

Analysis of scattering and absorption coefficients requires knowledge of particle index of refraction. Constant refractive indices of $1.95 - 0.66i$ for elemental carbon (Bergstrom, 1972) and $1.55 - 0.0i$ for organic carbon (Larson et al., 1988) were assumed. The wavelength-dependent complex index of refraction of Saharan dust particles described by Patterson et al. (1977) was assumed to be representative of dust present in Los Angeles. Optical properties of dust vary with location and even time, but few representative data are available. Fortunately, the contribution of dust to scattering and absorption was generally small, minimizing the uncertainty in derived optical properties resulting from this assumption. After calculation of the solute concentration of an aqueous salt aerosol, the refractive index is determined by the partial molal refraction approach of Moelwyn-Hughes (1961). For internal mixtures of salt and carbon, the volume-weighted average of the refractive indices of the components was used. Fuller et al. (1999) found that volume-weighted calculations tend to overestimate absorption of a mixed salt / elemental carbon particle relative to more physically realistic scenarios such as a salt shell that

contains an elemental carbon inclusion. However, because of uncertainty in the mixing state and size distribution of carbon in the aerosol, the magnitude of the error remains unknown. An ideal nephelometer would employ a Lambertian light source to directly measure the aerosol scattering coefficient. Real nephelometers do not measure scattering in near forward or near backward directions and have light sources that deviate from the ideal Θ dependence. Anderson et al. (1996) analyzed these non-idealities for the TSI 3563 nephelometer, and determined an angular sensitivity function, Θ , for both total scattering and hemispherical backscattering measurements. No similar data are available for the Radiance Research nephelometers, so their characteristics were assumed to be equivalent to those of the TSI instrument. We incorporated this angular sensitivity into the Mie theory calculations to predict the scattering coefficient expected to be measured by each of the nephelometers. Figure 2.6 shows closure comparisons with the total scattering coefficient measured by each of the Radiance Research nephelometers, the 550 nm hemispherical backscattering coefficient measured by the TSI nephelometer, and the absorption coefficient measured by the PSAP. Data from each of the seven flights during which filter samples were taken are included in the comparisons with the three nephelometers, while data from only those flights that included extended constant altitude legs were included in the PSAP comparison to minimize biases caused by pressure variations. Although each comparison is characterized by some discrepancy, that with the PSAP is clearly the most significant. Potential causes of this disagreement include errors in the analysis of carbon or in the distinction between organic and elemental carbon, errors in assumed mixing state and sphericity of the particles, and errors in the absorption measurement itself, potentially due to the broadside enhancement effect described by Fuller et al. (1999), in which branch-like carbon particles are preferentially oriented perpendicular to the filter surface and therefore the light source. It is unlikely that this discrepancy results from use of volume-weighted refractive indices in the size distribution-based calculations, since this would tend to increase the derived absorption coefficient, thereby improving agreement. It is not clear which, if any, of these potential errors is responsible for the disagreement. Hence, no modification of the assumptions used is warranted.

Deviations observed in these comparisons provide a rough estimate of the uncertainty in each of the measurements and, in particular, in the physicochemical description of the aerosol that will be used in analysis of the properties and impacts of the Los Angeles aerosol.

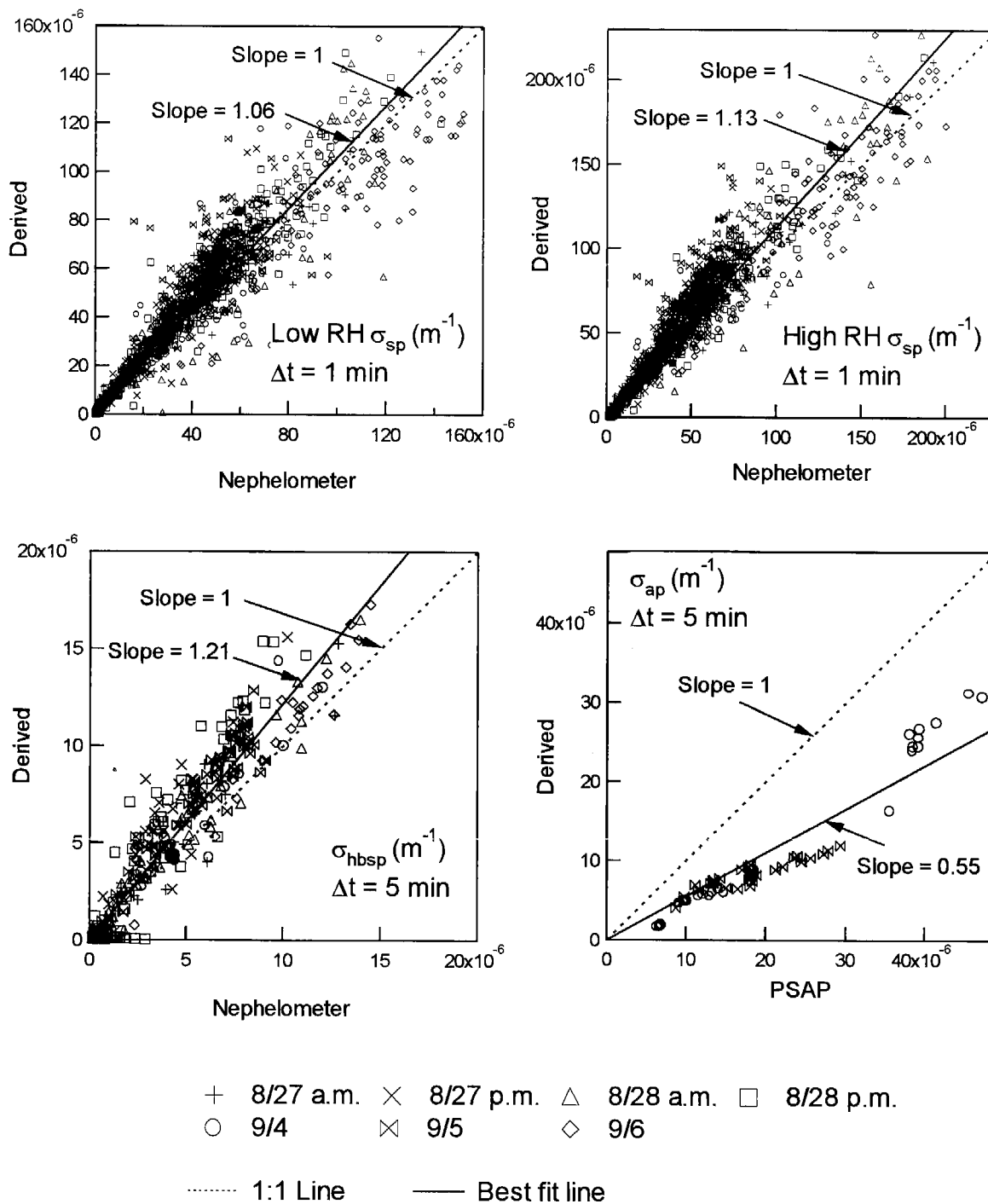


Figure 2.6 Closure comparisons between derived and directly measured optical properties. Data presented are from those flights during which filter samples were collected. Comparisons shown include total scattering coefficients measured by the Radiance Research nephelometers at varying relative humidity, hemispherical backscattering at 550 nm measured by the TSI nephelometer, and absorption measured by the PSAP.

3 Results and Discussion

3.1 Three-dimensional aerosol structure

A variety of flight patterns were utilized during SCOS97-NARSTO in order to explore the three-dimensional distribution of the aerosol in the Los Angeles Basin. Shown in Figure 3.1 is a flight pattern consisting of a sequence of ascending and descending spirals. This particular pattern was used during the first four missions of SCOS97-NARSTO. Both spatial and temporal variations in the aerosol were explored by conducting one of these 4-hour missions in the morning and another in the afternoon on both August 27 and August 28. Meteorological measurements showed the temperature inversion on August 27 had a height of approximately 350 m until breaking up in the early afternoon. A weak off-shore flow was observed during the evening, followed by on-shore flow and an inversion having a height of approximately 500 m the following day. Peak 1-hour ozone concentrations observed in the Southern California Air Basin were 116 and 132 ppb on August 27 and 28, respectively.

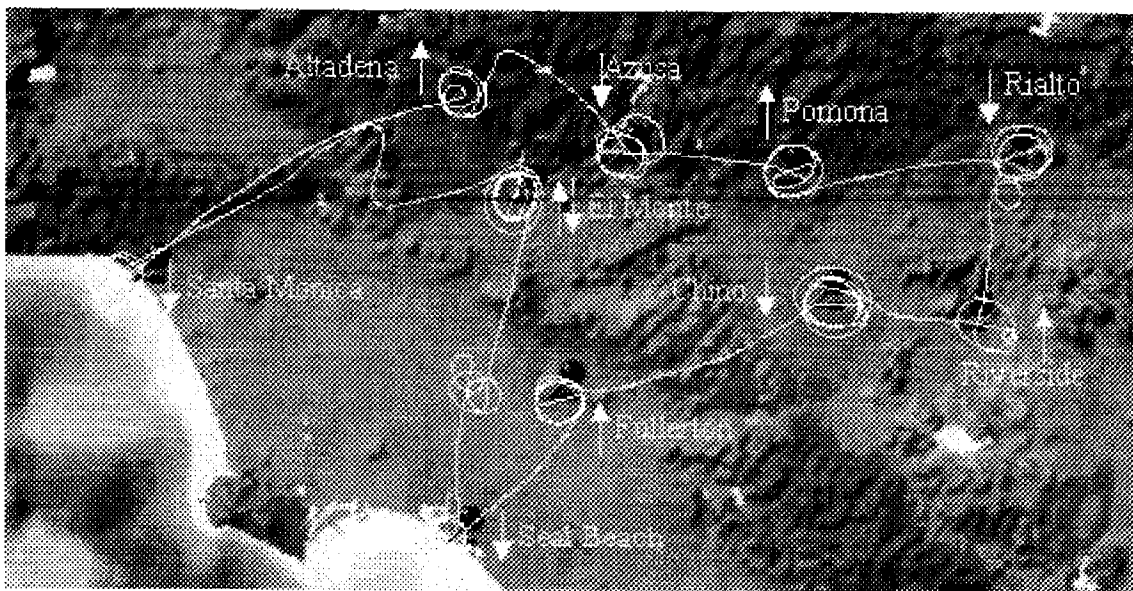


Figure 3.1 Flight pattern utilized during the first four missions (actual flight track from 8/27 a.m. mission is shown) to study the three-dimensional structure of the aerosol. Arrows indicate the direction(ascending or descending) of each spiral.

To present the three-dimensional structure of the aerosol during this period, data from spirals along two cross sections have been considered. An east-west cross section was chosen that includes spirals over Santa Monica, El Monte, Azusa, Pomona, and Rialto, while a north-south cross section includes spirals over Altadena, El Monte, Fullerton, and Seal Beach. It is not possible to completely deconvolute the spatial variations between spiral locations from variations that result from evolution or advection of the aerosol during the course of a flight. Nor is it possible to predict with confidence the aerosol properties at a point along one of the cross sections through simple interpolation of measurements made. Nevertheless, even with these

inherent sources of uncertainty, it is useful to present data along these cross sections as if they were snapshots in time exhibiting smooth variations between locations. Figures 3.2 and 3.3 present such a description of the aerosol sampled during flights on August 27 and August 28. PM_{2.5} has been considered here because of its regulatory relevance, although other descriptive parameters could have alternatively been used. Shown at the top of these figures are contour plots describing the near-ground level variation in aerosol mass throughout the study area. Also presented in these plots are the east-west (E-W) and north-south (N-S) cross sections used for the corresponding image plots shown below.

Collectively, the data presented in Figures 3.2 and 3.3 illustrate the characteristics and evolution of a late summer Los Angeles aerosol. Beginning on the morning of August 27, the aerosol was most concentrated over the inland valleys between El Monte and Chino, where PM_{2.5} exceeded $40 \mu\text{g m}^{-3}$. Strong gradients in PM_{2.5} are apparent along both cross sections between the coast and inland areas. Only a weak aerosol layer at approximately 1000 m above sea level (asl) is visible above the ground-level polluted layer. Along the east-west cross section, little change is observed in near-ground level aerosol mass from morning to afternoon, although the columnar aerosol burden over the inland areas increased, and a weak, but distinct, layer at ~ 400 m asl developed that stretches to Santa Monica. At approximately 1200 m asl along the north-south cross section, a much more intense aerosol layer is observed, in which PM_{2.5} exceeds $30 \mu\text{g m}^{-3}$. These data suggest that aerosol was injected above the mixed layer at the southern edge of the San Gabriel Mountains and was then transported away from the mountains with the sea breeze return flow. Aircraft-based measurements have previously identified such elevated pollution layers both over Southern California (Blumenthal et al., 1978; Wakimoto and McElroy, 1986; Li et al., 1997), as well as over similar coastal regions (Wakamatsu et al., 1983; Lalas et al., 1983; Hoff et al., 1997). A second, less pronounced, layer is present approximately 200 m above the first. The two layers present along the east-west cross section the following morning are likely remnants of this (these) layer(s). As the ground-level mixed layer deepens in the afternoon of August 28, the morning layers cease to be distinct, suggesting that they mixed with the underlying layer. Along the north-south cross section, an elevated layer formed on August 28 in much the same way as was observed the previous day.

The climb and descent rates used during this study were typically 150 m min^{-1} , leading to a vertical resolution of ~ 150 m in the size distribution measurements. This was usually sufficient to capture the aerosol structure. However, aliasing due to this limited vertical resolution became significant during several spirals. Nephelometer measurements that were obtained with 6 s resolution were used in these instances to characterize the sharp variations present. Figure 3.4 shows vertically-resolved aerosol scattering coefficients recorded with the non-humidified Radiance Research nephelometer during each of the spirals flown off the coast of Santa Monica on the first four flights. The morning spirals showed relatively little vertical variation on either day. With the strengthening of the sea breeze in the afternoon, pronounced, but thin (~ 100 m), aerosol layers developed. The scattering coefficient of 0.00014 m^{-1} measured in the August 28 layer was among the highest observed at any location during the study. Like the layers over the inland areas, these coastal layers have been observed in previous studies and are attributed to vertical transport along the heated coastal ranges, followed by horizontal transport towards the coast as part of the sea breeze return flow (Lu and Turco, 1994).

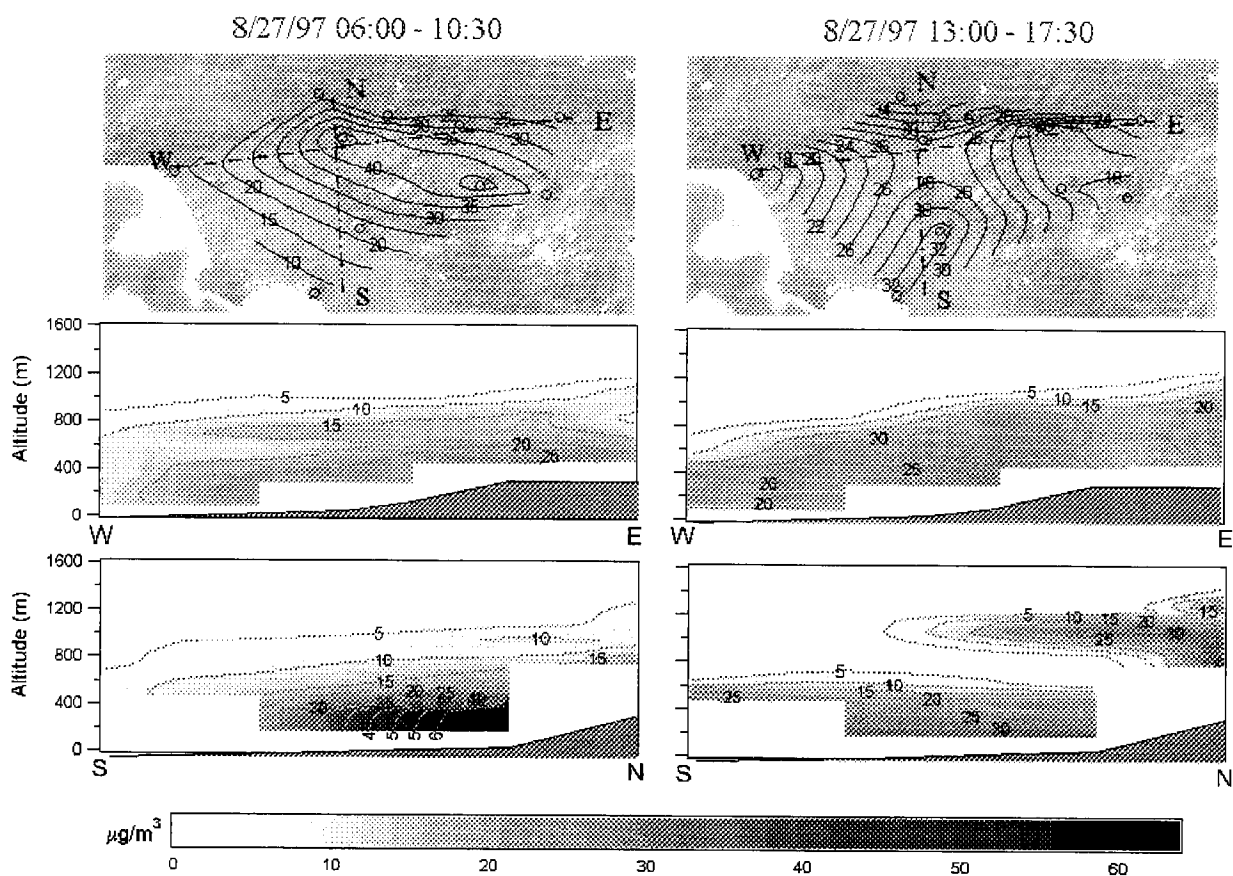


Figure 3.2 Distribution of PM_{2.5} throughout the Los Angeles basin as sampled during morning and afternoon flights on August 27. The top plots show contours of near-ground level aerosol mass as well as the east-west (E-W) and north-south (N-S) cross sections used in the image plots shown below. Represented in the image plots is PM_{2.5} interpolated from adjacent spirals. The solid grey area at the bottom of each of the image plots represents the approximate ground level.

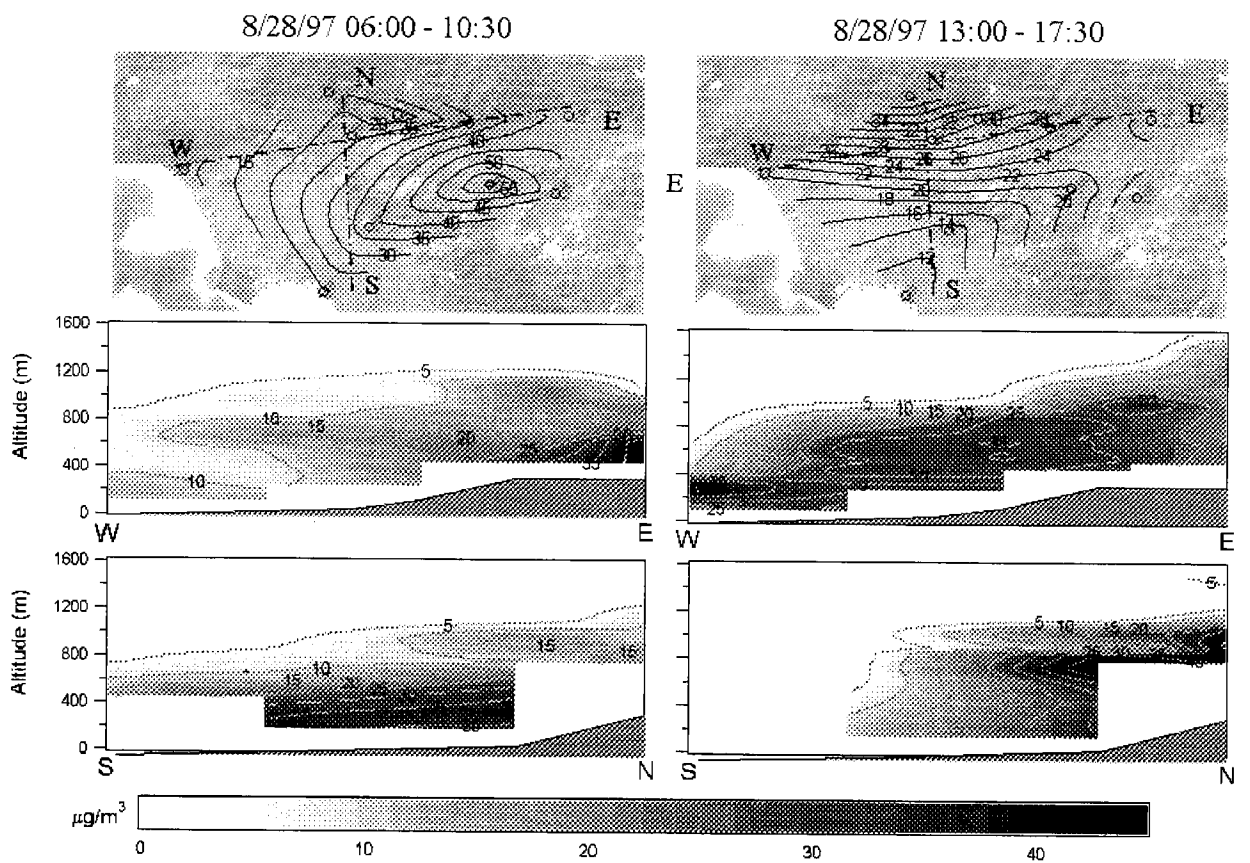


Figure 3.3 The same format as in Figure 3.2 for the aerosol sampled during morning and afternoon flights on August 28.

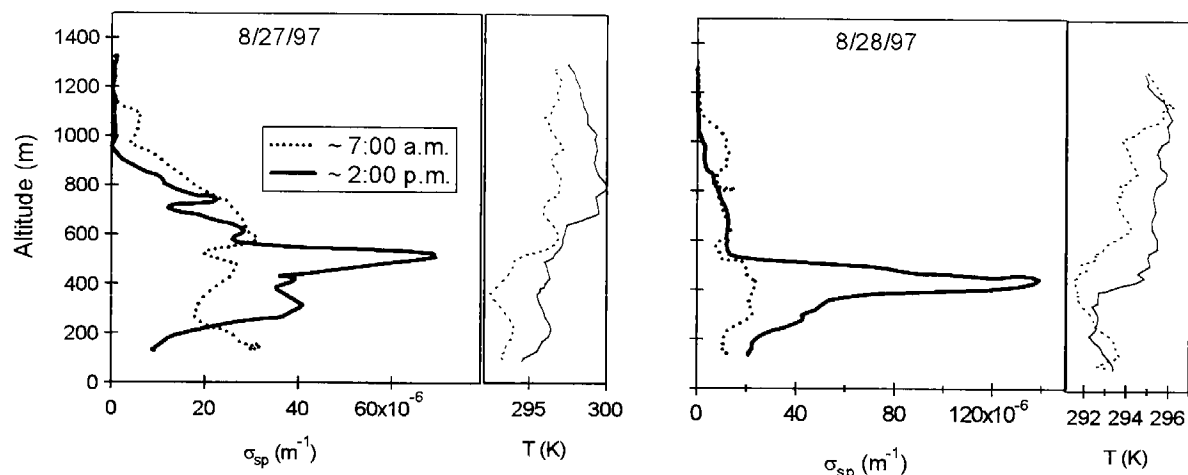


Figure 3.4 Vertical profiles of ambient temperature and aerosol scattering coefficient measured during spirals flown off the coast of Santa Monica on four missions conducted on August 27 and 28.

The spirals flown during the four missions discussed above, and during most of the other eight missions, focused on the aerosol present in approximately the lower 1500 m of the atmosphere. However, several spirals reached altitudes of over 3000 m during one flight on September 9 and two flights the following day. On both of these days upper level winds were from the south and west, and temperature inversions were present until breaking in the mid-afternoon. Maximum 1-hour ozone concentrations were 105 and 113 ppb on September 9 and 10, respectively. In all, three of these spirals were flown over El Monte and two over Long Beach. Though the spirals were flown over a 32-hour period at two dissimilar locations, each encountered an aerosol layer at approximately 2500 m having a peak PM_{2.5} mass of about $2 \mu\text{g m}^{-3}$. Figure 3.5a presents vertical profiles of PM_{2.5} that show the relative magnitudes of these elevated layers. The early morning spiral flown over El Monte on September 9 indicates that a more concentrated layer may have been present above 3000 m, although no similar layers were observed during 3400 m spirals on the morning of September 10. The averaged mass distributions for the layers indicated by arrows in Figure 3.5a are presented in Figure 3.5b. This figure shows a clear shift in the aerosol mass distribution within the 2500 m layer relative to the aerosol within either the ground level or 1500 m layers. This observation is consistent with an aerosol that has aged through condensation and coagulation. The importance of this elevated layer will be considered in the discussion of photolysis rates below.

Seven different flight patterns were employed for the twelve missions flown during SCOS97-NARSTO, making analysis of day-to-day variations difficult. However, the majority of flight patterns included spirals over El Monte, Riverside, and Fullerton. These repeated spirals provide the data necessary for a statistical analysis of the aerosol over these locations. Day to day variations in the aerosol concentration and properties obscured any diurnal trends that might otherwise have been apparent. Therefore, in combining data from each set of spirals, no distinction was made between samples taken at different times. Figure 3.6 presents the mean and standard deviation of several intensive and extensive aerosol properties as a function of altitude for 10 spirals flown over both El Monte and Riverside, and 9 flown over Fullerton. The data have been smoothed to more clearly show vertical trends. As indicated in these plots, the aerosol

variability at each location exceeds the mean variability between locations. Consistent with expectations, aerosol mass and concentration decrease with increasing altitude. Also consistent with expectations, aerosol mass increased with distance traveled inland from Fullerton, which is approximately 20 km from the coast, to Riverside, which is near the eastern edge of the Los Angeles Basin. Aerosol number concentrations at El Monte were, on average, about 50% greater than at Riverside, indicating that much of this increased mass results from growth of existing particles.

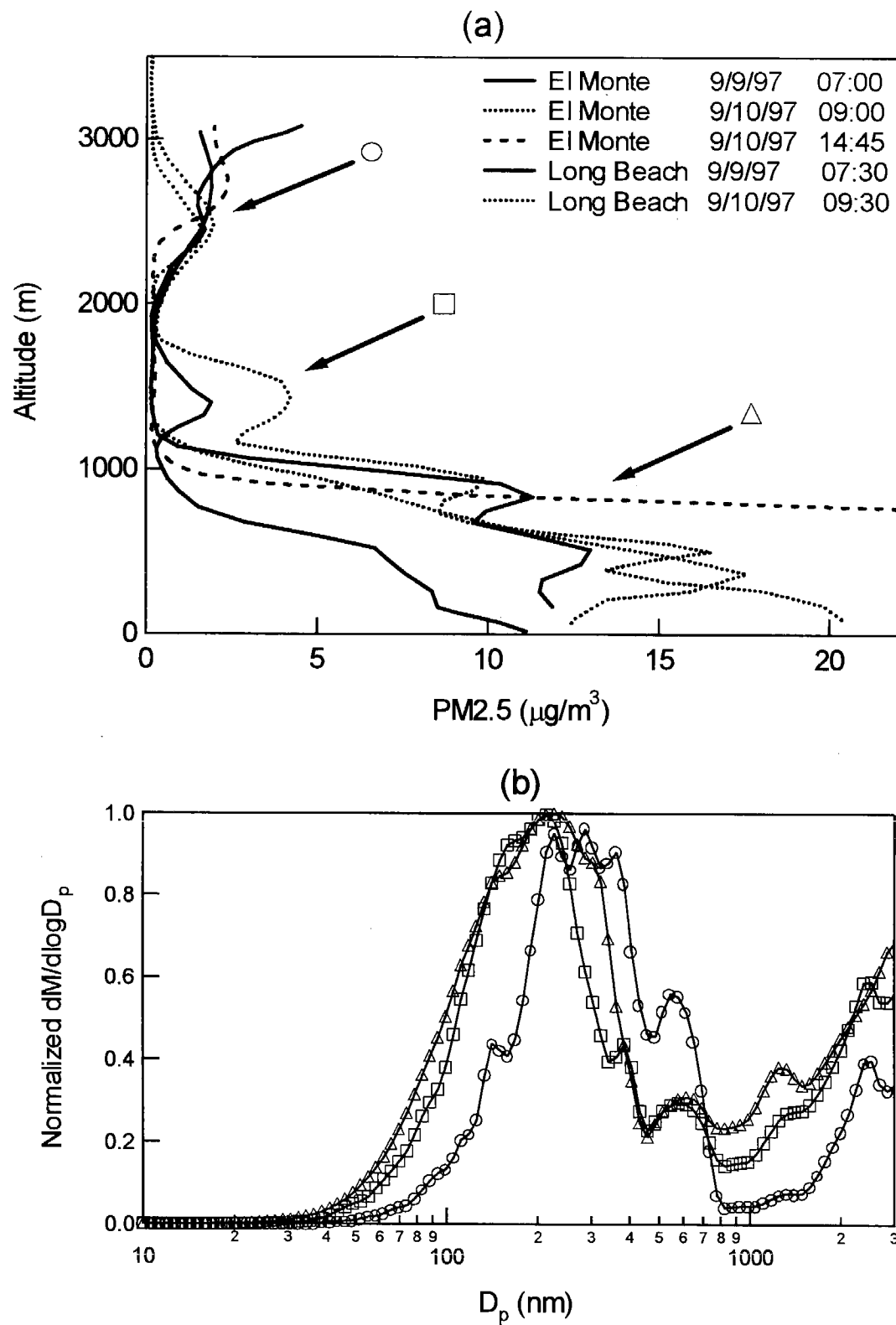


Figure 3.5 (a) Vertical profiles of PM2.5 measured during 3000+ m spirals flown over El Monte and Long Beach, and (b) normalized mass size distributions averaged over each of the layers indicated by arrows in (a).

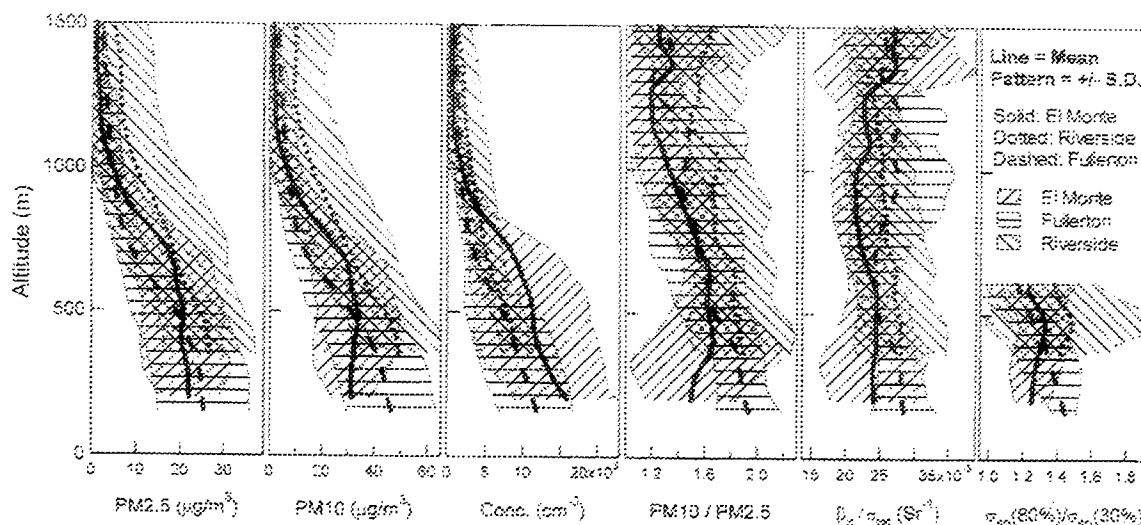


Figure 3.6 Vertical profiles representing the mean and standard deviation of a number of extensive and intensive aerosol properties. Data taken during the ten flights during which spirals were flown over El Monte and Riverside, and nine flights with spirals flown over Fullerton were used in the analysis. For the derived ratio of scattering at 80% RH to scattering at 30% RH, only those data below the altitude at which random error began to dominate are shown.

Steadily improving air quality in Los Angeles, coupled with atypical meteorology associated with a strong El Niño event, led to significantly lower aerosol loadings during SCOS97-NARSTO than during SCAQS ten years earlier. However, the relative contributions of fine (PM_{2.5}) and coarse (PM₁₀ - PM_{2.5}) fractions remained much the same. Chow et al. (1994) found that, during SCAQS, PM_{2.5} constituted between 50 and 67% of PM₁₀, while near-ground level measurements made on board the *Pelican* during SCOS97-NARSTO indicate a corresponding range of 53 to 69%. At each of these locations, PM_{2.5} constituted an increasing percentage of PM₁₀ with increasing altitude. Also shown in Figure 3.6 is the vertical variation of the calculated radar backscattering to extinction ratio that is used for evaluation of lidar data. The wavelength considered, 355 nm, is that used by a lidar operated in El Monte during SCOS97-NARSTO. The observed spatial, temporal, and altitude dependent variability bounds the uncertainty caused by assuming a constant or simple altitude-dependent ratio when estimating aerosol extinction from raw lidar signals. The ratio of aerosol scattering at 80% RH to that at 30% RH is derived using the data from the Radiance Research nephelometers along with Equation (2.1). Only those data below the altitude at which random error began to dominate this ratio are shown. The enhanced ratio observed for Riverside suggests that aerosol hygroscopicity is greater in the inland areas, although variations in aerosol size distribution could also account for the change.

The overall picture that has been obtained from these airborne observations is of a highly complex vertical aerosol distribution rather than a simple mixed layer in contact with the ground and trapped below a temperature inversion. The observations are, however, at least qualitatively consistent with three-dimensional modeling results of the Los Angeles area (e.g., Lu and Turco, 1995).

3.2 Trajectory studies

Identical patterns were flown on September 4 and 5 as part of an intensive measurement period during SCOS97-NARSTO that was designed to investigate nitrate formation along a trajectory beginning east of downtown Los Angeles in Diamond Bar, passing over the ammonia-rich area near Mira Loma, and ending near the eastern edge of the Los Angeles Basin in Riverside. Meteorological measurements described an initial offshore flow on September 4 that gave way to onshore winds and a 120-150 m deep marine layer on September 5. This transition was largely the result of increasing influence of tropical storm Kevin off the tip of the Baja peninsula. Peak 1-hour ozone concentrations diminished with this transition from 157 ppb on September 4 to 113 ppb on September 5. To ensure a sufficient amount of aerosol was collected for filter analyses, the *Pelican* circled ~300 m above each sampling site for approximately one hour. Figure 3.7 shows both the flight patterns for these missions and the calculated back trajectories for air parcels arriving at Mira Loma and Riverside during the corresponding sampling intervals. Each mark on the back trajectories represents 1 hour. Wind fields used for the trajectory calculations were constructed according to the methods of Goodin et al. (1979) and Harley et al. (1993) using hourly averaged wind speed and direction at 29 meteorological stations maintained by the South Coast Air Quality Management District. Back trajectories calculated for the sampling times during the September 4 flight indicate nearly stagnant conditions, making any analysis that assumes the same air masses were sampled at each location meaningless. Back trajectories calculated for the September 5 flight show that air masses sampled at the downstream locations were also separated temporally and spatially from those sampled earlier in the flight, but this separation was not as extreme as on the previous day, and does not preclude an analysis of the variations between locations.

During the September 5 flight, 37.3, 35.8, and 22.1 $\mu\text{g m}^{-3}$ of fine aerosol mass was collected on filter samples taken over Diamond Bar, Mira Loma, and Riverside, respectively. The decrease in aerosol mass with distance along the trajectory suggests a deepening mixed layer or advection that dilutes the aerosol population. Therefore, to describe nitrate formation within this pseudo air mass, it is useful to normalize the nitrate concentration in some manner. Although normalizing with respect to total mass may provide a reasonable estimate of the relative contribution of nitrate, it is possible that additional species such as sulfates and secondary organic aerosol are also formed along the trajectory. Since primary aerosol emissions are most concentrated in the downtown Los Angeles area, it is likely that the black carbon present in the aerosol is derived primarily from these upwind sources. Therefore, black carbon can be considered as a somewhat conserved quantity. Hence, for this analysis, fine nitrate (as well as other species) mass was normalized to fine elemental carbon mass. The mass ratio of nitrate to EC was 5.3, 9.5, and 7.3, and that of ammonium to EC was 2.3, 3.6, and 3.0 for the Diamond Bar, Mira Loma, and Riverside samples, respectively. The molar ratio of the change in nitrate to the change in ammonium was 0.94 and 1.1 between Diamond Bar and Mira Loma, and Mira Loma and Riverside, respectively, suggesting that it was ammonium nitrate that was gained or lost from the aerosol. The 80% increase in normalized nitrate between Diamond Bar and Mira Loma is consistent with expectations of ammonium nitrate formation over this agricultural region that has high ammonia emissions. However, the cause of the observed decrease in nitrate contribution to the aerosol between Mira Loma and Riverside is not apparent. It is likely that differences in air masses sampled at each location are responsible for this unexpected result, a speculation that is supported by observed concentration gradients during these flights as will be

discussed in the following section.

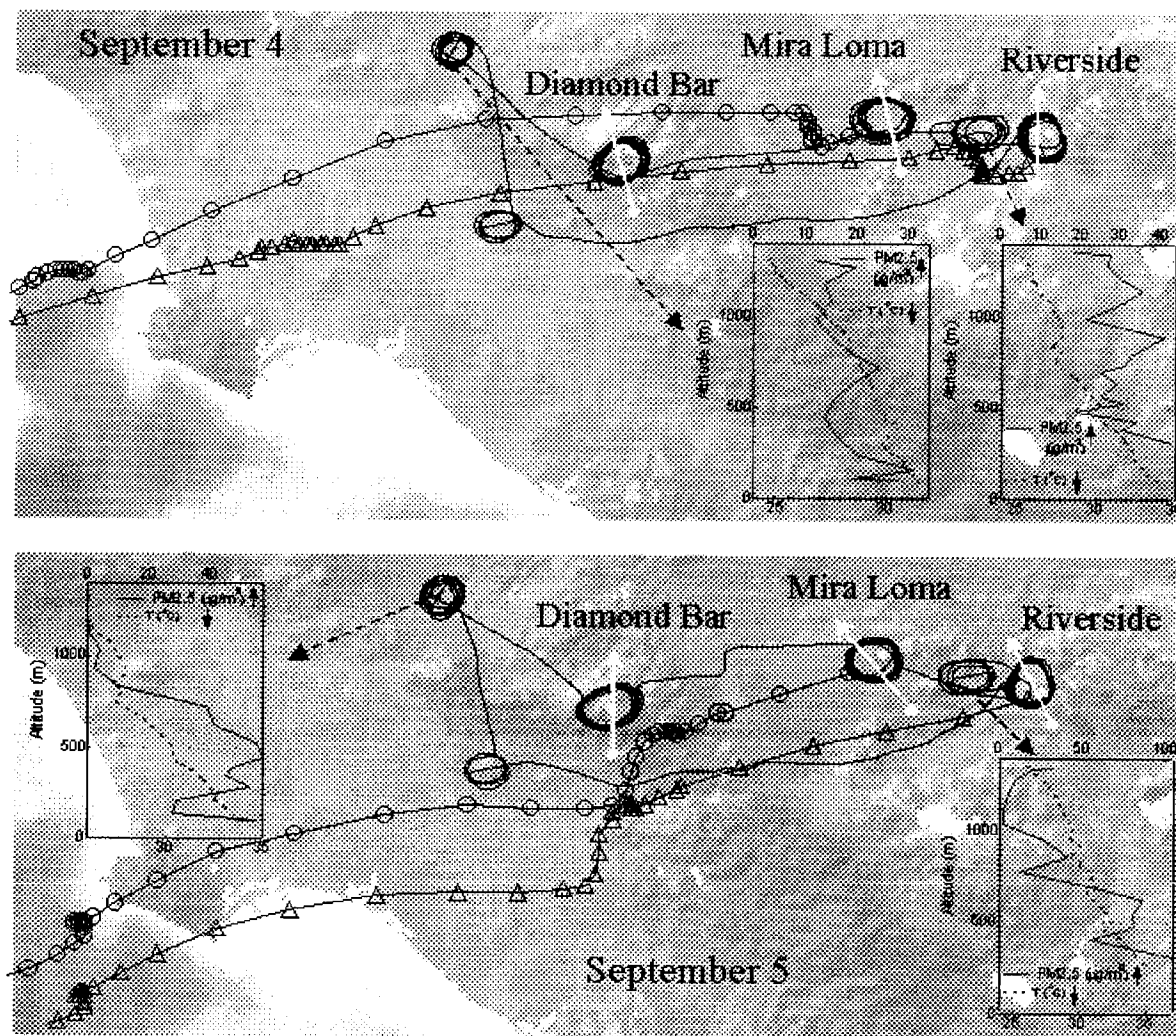


Figure 3.7 Flight patterns for missions conducted on September 4 and 5, along with calculated back trajectories for air parcels arriving at Mira Loma and Riverside during the corresponding sampling intervals. Insets show vertical profiles of PM2.5 and temperature at spiral locations. The heavy horizontal line in each of the profiles represents the approximate altitude of the circles flown above Diamond Bar, Mira Loma, and Riverside. The solid arrows through the flight track represent the direction of maximum aerosol gradient at each of the sampling locations that was used for the analysis presented in Figures 3.8 and 3.9.

3.3 Sub-grid variability

The primary goal of SCOS97-NARSTO was the acquisition of a sufficiently detailed database to lead to effective evaluation of photochemical and aerosol modeling capabilities. Computational limitations, sparse meteorological and air quality measurements, and limited emissions inventories all serve to limit the minimum useful computational grid size of three-dimensional models. Typical grid cells are 5 km on a side with a vertical dimension that varies with height (Meng et al., 1997). McNair et al. (1996) discuss potential errors involved in assuming that point measurements of a given species represent the grid cell volume-average. In their analysis of data obtained during SCAQS, they found that for the one pair of monitoring sites that were separated by less than 5 km (4.8 km), variations in peak ozone concentration of up to 50% were observed. Similar discrepancies were noted when point measurements were compared with interpolations between surrounding measurements.

Inspection of data from these flights during some of the constant altitude circular flight patterns showed persistent gradients in aerosol concentration. The diameter of the circles ranged from about 5.5 to 6.5 km. This is comparable to the computational grid size of conventional three-dimensional models. Unlike simultaneous ground-based samples at multiple locations, airborne analysis of relative changes in pollutant concentrations is largely insensitive to instrumental variability. On the other hand, with aircraft sampling it is possible that variations perceived as being attributable to horizontal gradients could, in fact, result from sampling along the boundary of a vertical layer that varies in height. Because of flight pattern restrictions, spirals were not flown over any of the sampling locations, but were flown above adjacent areas. As shown in the insets in Figure 3.7, vertical profiles of PM_{2.5} and temperature over El Monte and Riverside do not indicate the presence of sharp vertical gradients near the sampling altitude (~500 m), suggesting that any variations are horizontal in nature.

For each sampling location shown in Figure 3.7, an arrow indicates the direction corresponding to the maximum gradient in aerosol concentration. Figures 3.8 and 3.9 show variations along the indicated direction of maximum gradient of several normalized extensive and intensive aerosol properties, as well as size distributions. The data along the gradients were averaged to limit scatter. Some variability was apparent at each location, but that observed at Diamond Bar and Mira Loma on September 4 and Riverside on September 5 is consistent with the presence of strong gradients in aerosol concentration, resulting in PM_{2.5}_{max}:PM_{2.5}_{min} ratios of 1.61, 1.33, and 1.39, respectively. The lack of variability in either the intensive properties or the shape of the size distributions suggests that the aerosol concentration varies with location, but its characteristics do not. As is true for most of the Los Angeles Basin, there are major freeways as well as other potential emissions sources in the vicinity of each of these locations. It is not, however, possible to state conclusively that they are responsible for the variability. It is interesting to note that none of the locations exhibited the same variability, or lack thereof, on both days. Additional measurements are necessary to determine whether the presence of these strong gradients follows a diurnal pattern, which might explain the differences observed over the two-day period since the September 4 mission was conducted approximately four hours earlier than the flight conducted on September 5.

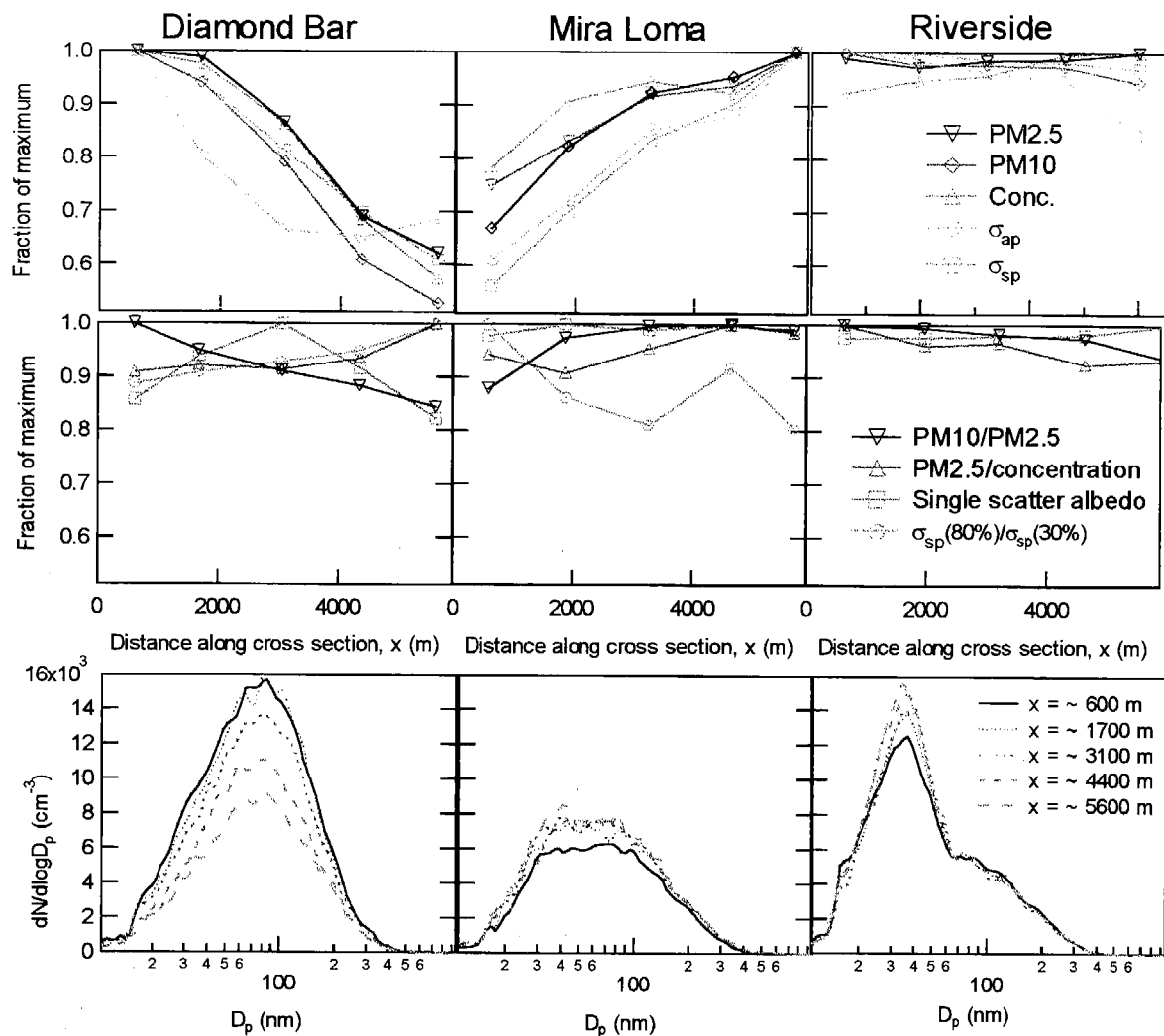


Figure 3.8 Variation of extensive aerosol properties, intensive aerosol properties, and number size distributions as a function of distance along the direction of maximum gradient indicated in Figure 3.7.

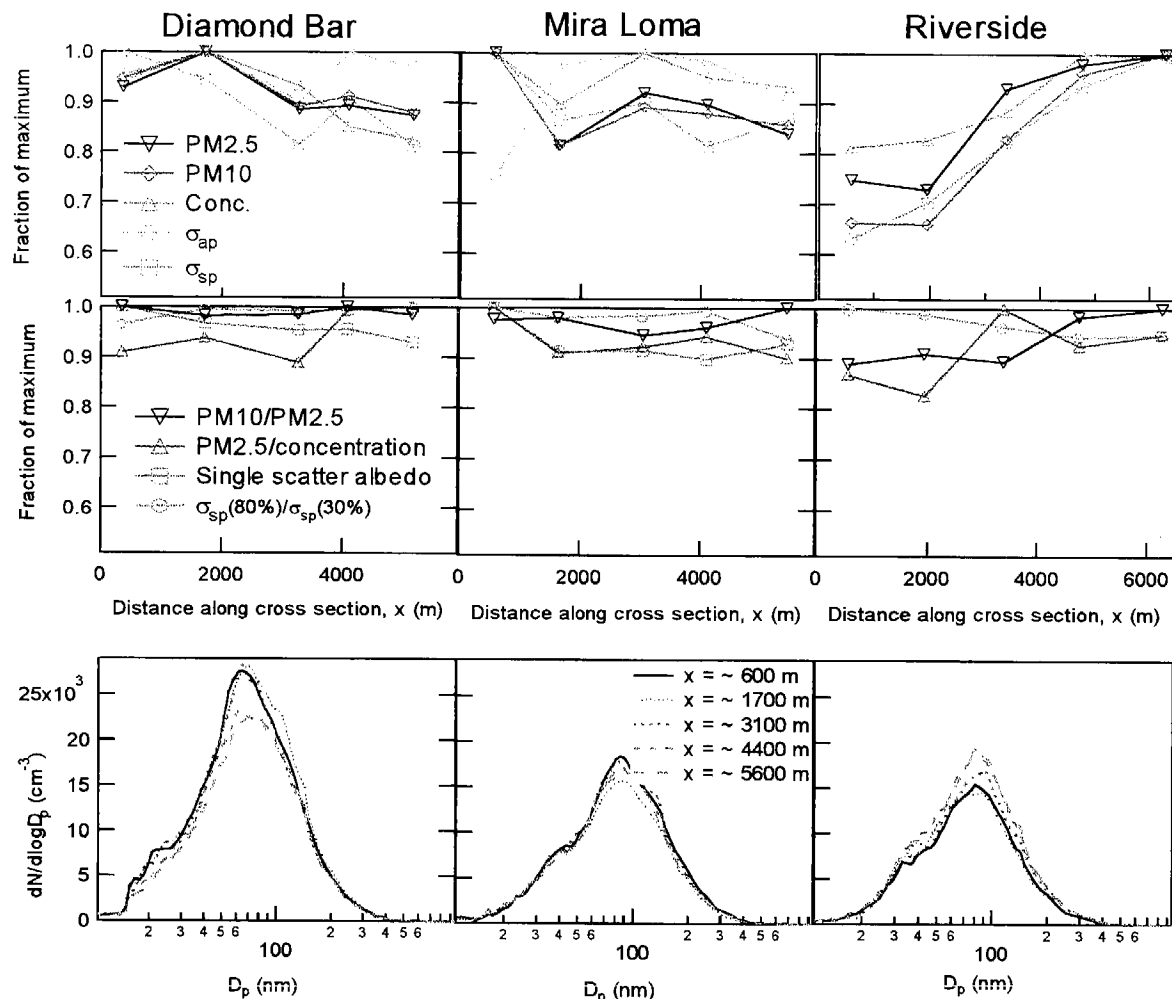


Figure 3.9 The same format as in Figure 3.8 for the aerosol sampled on September 5.

3.4 Effect of the aerosol on photolysis rates

Formation of ozone and a number of other gas and aerosol phase species is driven by photochemistry (Seinfeld and Pandis, 1998). Accurate prediction of gas-phase concentrations requires a detailed understanding of the array of reactions responsible for their formation and destruction, as well as the spectrally-resolved actinic flux throughout the area of interest. Direct measurement of actinic flux or key photolysis rates themselves can provide the necessary information, although such data are typically available only at ground-level. Alternatively, vertical aerosol profiles derived from airborne measurements or vertically-resolved models can be used to determine the potential impact of scattering and absorption on photolysis rates. Several investigations of this type have been reported for different regions with varying cloud cover, surface albedo, and solar zenith angle (Demerjian et al., 1980; Ruggaber et al., 1994; Lantz et al., 1996; Castro et al., 1997; Dickerson et al., 1997; Jacobson, 1998; Liao et al., 1999). The extensive aerosol measurements made with the *Pelican* provide much of the data necessary for such an analysis, thereby reducing uncertainty in the role of the aerosol in atmospheric photochemistry.

The approach taken to determine photolysis rates has been described in Liao et al. (1999), and will be described only briefly here. Actinic flux was calculated using the one-dimensional discrete ordinate radiative transfer (DISTORT) model (Stamnes et al., 1988). The calculations employed eighty vertical layers from 0 to 70 km that ranged in thickness from 100 m in the lowest 3 km, to 5 km between 50 and 70 km in altitude. Aerosol concentration was assumed to be zero above the maximum measurement height. Clearly, this will result in some error in derived photolysis rates. An analysis of the impact of the layers observed at about 2500 m will be discussed below, but no consideration of even higher layers is made, although it is likely that the aerosol present above this height contributes negligibly to the columnar aerosol burden. Actinic flux was calculated for the 290 to 700 nm wavelength range with spectral intervals ranging from 1 nm for wavelengths between 290 and 330 nm, to 5 nm between 600 and 700 nm. Published data for temperature-dependent ozone absorption cross section (Malicet et al., 1995; WMO, 1985), solar irradiance (Neckel and Labs, 1984; Woods et al., 1996), temperature profile (Nagatani and Rosenfield, 1993), ozone profile (McPeters, 1993), and spectrally-resolved surface albedo (Demerjian et al., 1980) were utilized for these analyses. As is common in Southern California during the summer months, clouds were rare during this study and were, therefore, not considered. To clearly demonstrate the variability associated with aerosol concentration and properties, and not time of day, a constant solar zenith angle of 10° was considered.

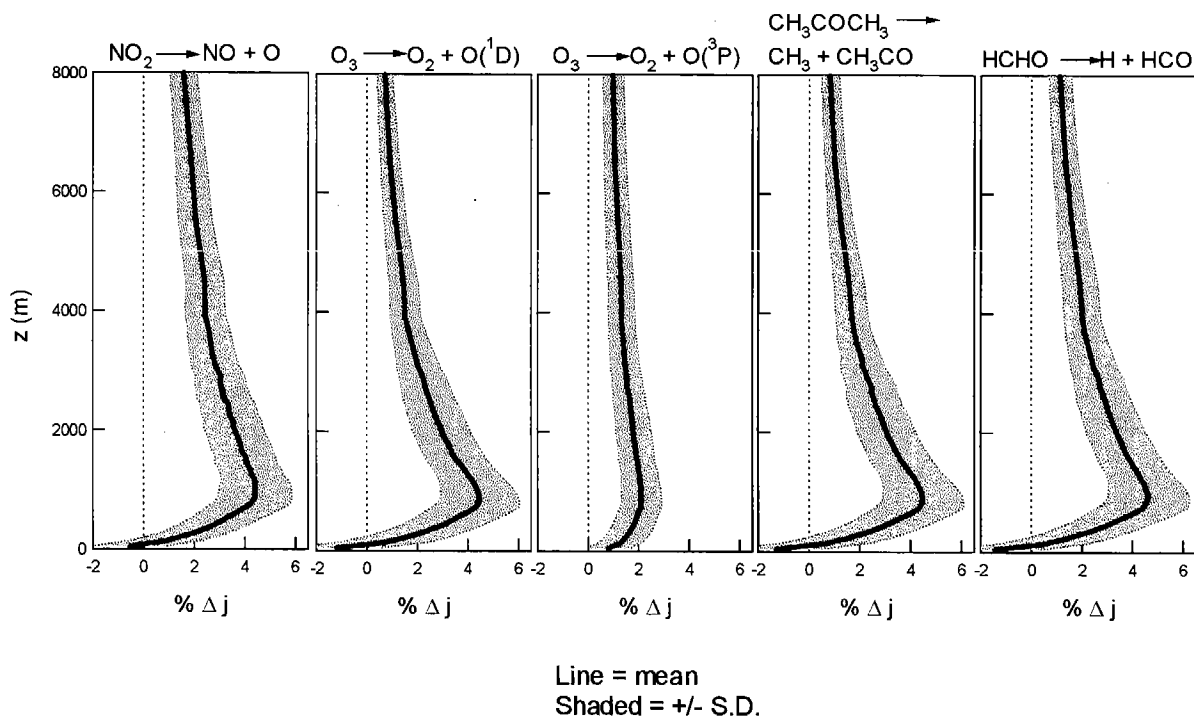


Figure 3.10 Fractional change in five gas-phase photolysis rates calculated to have resulted from the aerosol sampled over El Monte relative to an aerosol-free atmosphere. For each reaction considered, the mean and standard deviation were determined from photolysis rate calculations using measurements made during spirals flown over El Monte on ten flights. Unlike most of the other analyses presented here, altitude is relative to ground level and not sea level.

Consistent with the approach taken to characterize physical and chemical aerosol properties, photolysis rates were computed based on data taken along a cross section during one flight, and taken at one location during several flights. The fractional change in several key photolysis rates resulting from the aerosol sampled over El Monte during 10 flights is presented in Figure 3.10. As with the statistical analysis of vertically-resolved aerosol properties shown in Figure 3.6, the mean and standard deviation were calculated and presented as a solid line and shaded region, respectively. Little variation is observed in the impact the aerosol is expected to have on photolysis rates of NO_2 , HCHO , CH_3COCH_3 , and $\text{O}_3 \rightarrow \text{O}(^1\text{D})$, while the impact on photolysis of O_3 to form $\text{O}(^3\text{P})$ is smaller in magnitude and exhibits less vertical variability than is observed for the other reactions considered. For each reaction analyzed, the El Monte aerosol causes a slight decrease in photolysis rates in the lowest 100 m, with a more pronounced enhancement observed above this height. The presence of a cross-over point at which the fractional change of a given photolysis rate is zero results from an offset between increased diffuse actinic flux due to aerosol-enhanced scattering and decreased direct actinic flux caused by upward scattering and absorption by the overlying aerosol. These cross-overs have been observed in similar analyses with relatively non-absorbing aerosol like that encountered during SCOS97-NARSTO (e.g., Liao et al., 1999).

The maximum increase in photolysis rates above that expected if no aerosol were present is approximately 2% for $\text{O}_3 \rightarrow \text{O}(^3\text{P})$, and 5% for each of the other reactions considered. Inclusion of the 2500 m aerosol layers measured during spirals over El Monte on September 9 and 10 results in a further enhancement of approximately 1% (0.3% for $\text{O}_3 \rightarrow \text{O}(^3\text{P})$). Similar results were obtained when the fractional change in the photolysis rate of NO_2 was considered along the east-west cross section described in Figure 3.3 using data from morning and afternoon flights on August 28. As shown in Figure 3.11, only slight variations in photolysis rate alteration are observed along the cross section, both in the morning and afternoon. The sharp gradient in fractional photolysis rate change with height in the lowest 500 m demonstrates the potential error caused by extrapolations of ground-based radiative flux measurements. The impact of aerosols on photolysis rates presented here is similar to estimates of Jacobson (1998) using data obtained over Long Beach on August 27, 1987 during SCAQS, but differs significantly from calculations performed using data obtained over Claremont on the same day. Specifically, Jacobson (1998) predicted that the aerosol present over Claremont resulted in a decrease of up to about 12% in the NO_2 photolysis rate, resulting from a more concentrated and highly absorbing aerosol than was sampled during SCOS97-NARSTO. The atypical meteorological conditions during this campaign prevented a comparable severe pollution episode, while improved air quality in Southern California since 1987 would probably limit the likelihood of aerosol loadings similar to those observed in Claremont during SCAQS. Therefore, the results from SCOS97-NARSTO and SCAQS probably bound the likely impact that a significant, present-day, pollution episode would have on photolysis rates.

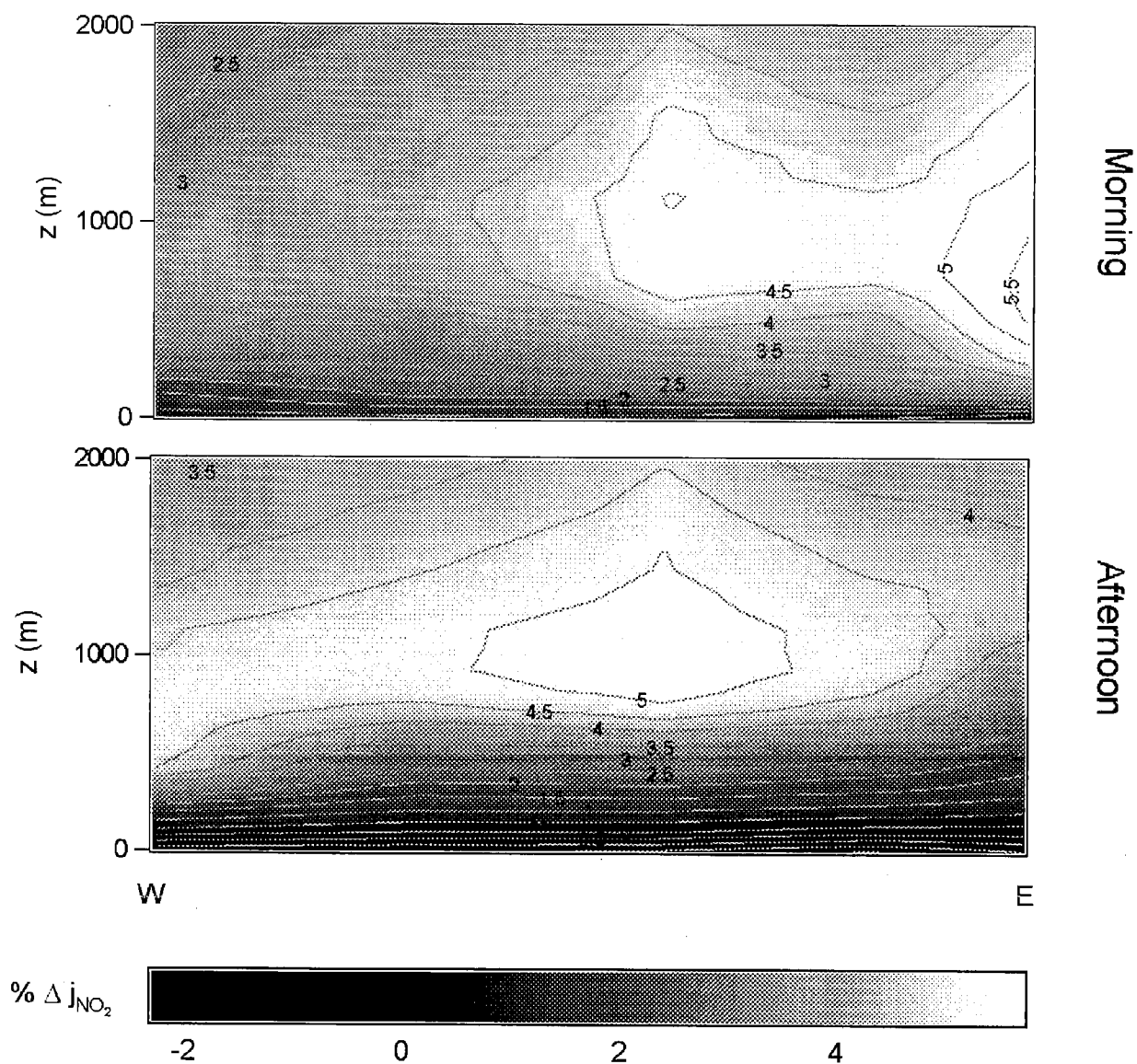


Figure 3.11 Vertically-resolved fractional change in the NO_2 photolysis rate calculated using data obtained during spirals flown on the morning and afternoon flights of August 28. The east-west cross section indicated in Figure 3.3 was used for presentation of these data.

4 Summary and Conclusions

As part of the SCOS97-NARSTO, 12 missions were conducted with an aircraft instrumented to characterize the chemical and physical properties of the Los Angeles aerosol. Instrumentation on board included three parallel filter sampling systems, three nephelometers, an absorption photometer, a DMA, and two OPCs. Data from the variety of measurements made were combined to provide a time-resolved physicochemical description of the aerosol. Several closure comparisons were performed between derived and directly measured properties. Best-fit lines through scatter plots containing these data for comparisons of fine aerosol mass, "dry" aerosol scattering coefficient, "wet" aerosol scattering coefficient, hemispherical backscattering coefficient, and absorption coefficient had $\frac{\text{derived}}{\text{measured}}$ slopes of 0.91, 1.06, 1.13, 1.21, and 0.55, respectively. The exact cause of the large disagreement in the absorption comparison is not known, although a number of potential errors have been suggested.

The aerosol present over the Los Angeles Basin exhibits a complex three-dimensional structure. Vertically-resolved data suggest that pronounced elevated layers present over the inland areas were formed through injection of aerosol above the ground-level polluted layer along the Southern edge of the San Gabriel Mountains, followed by advection towards the coast through incorporation into the sea breeze return flow. Additional layers were observed about 500 m asl off the coast of Santa Monica, and approximately 2500 m asl over El Monte and Long Beach. Data from spirals flown over El Monte, Fullerton, and Riverside on several flights over the three-week sampling period were used to provide a limited statistical description of the vertically-resolved aerosol at each location. In general, it was found that variability over time exceeded variability among locations. Constant altitude circles flown over Diamond Bar, Mira Loma, and Riverside yielded evidence of gradients in aerosol concentration sufficient to cause over 50% variability within a 5 x 5 km computational grid cell commonly used in atmospheric models.

Data from spirals flown over El Monte during several flights, as well as from spirals flown over several locations on August 28, were used to analyze the impact of the aerosol on important photolysis rates in the photochemical generation of ozone. On average, the aerosol was predicted to cause a slight decrease in photolysis rates in the first 100 m above ground-level, but led to a more pronounced (up to ~5%) increase above that height. For most of the reactions considered, the 2500 m elevated aerosol layers above El Monte caused an enhancement in photolysis rates of about 1% above that resulting from the aerosol present below these layers. Collectively, the data obtained in this sampling program provide further insight into microphysical processes that govern the size, composition, and spatial and temporal behavior of the Los Angeles aerosol.

References

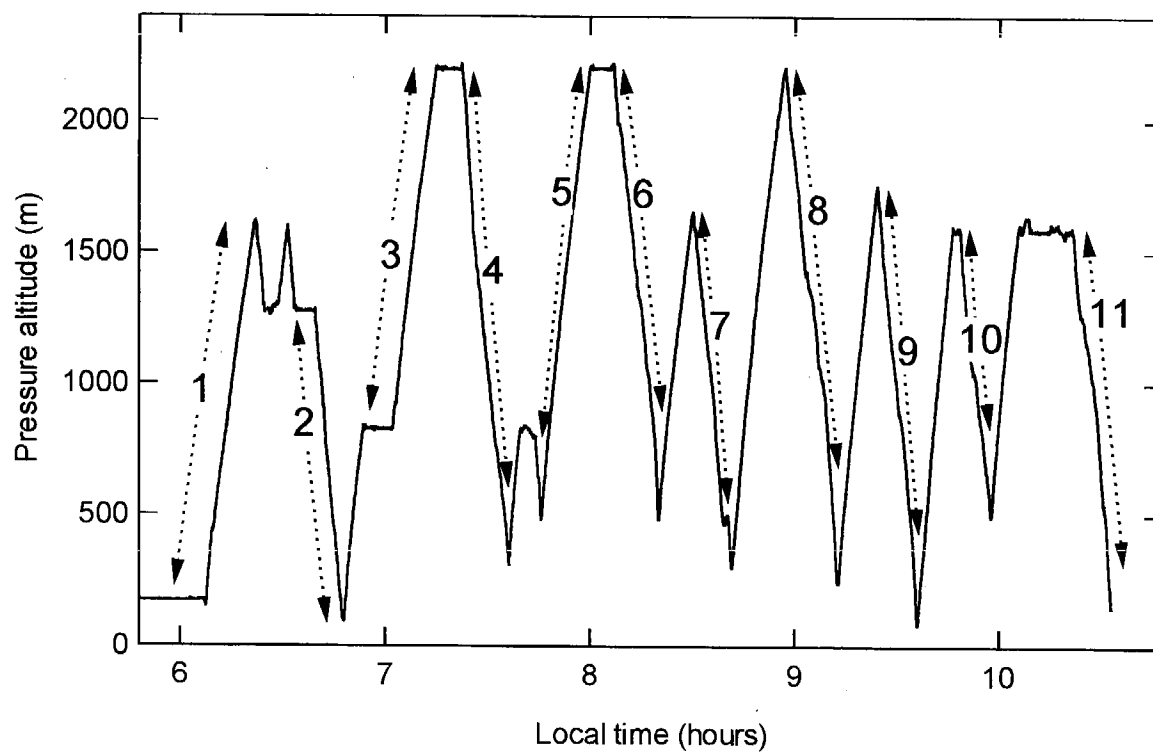
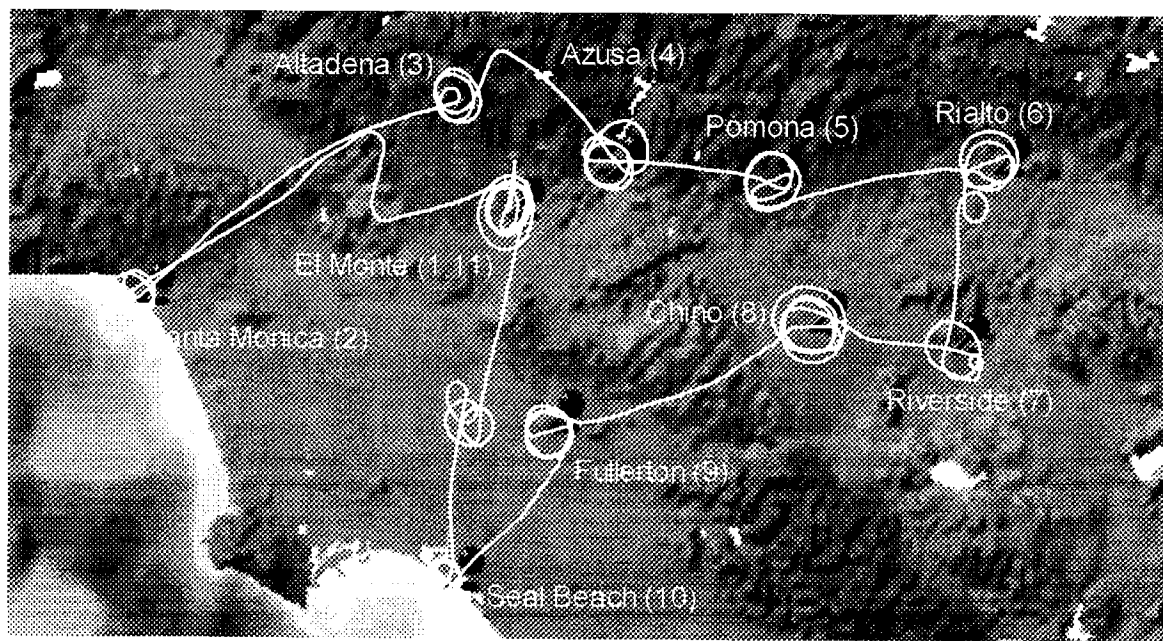
- Anderson, T. L., D. S. Covert, S. F. Marshall, M. L. Laucks, R. J. Charlson, A. P. Waggoner, J. A. Ogren, R. Caldwell, R. L. Holm, F. R. Quant, G. J. Sem, A. Wiedensohler, N. A. Ahlquist, and T. S. Bates, Performance Characteristics of a High-Sensitivity, Three- Wavelength, Total Scatter/Backscatter Nephelometer, *Journal of Atmospheric and Oceanic Technology*, 13, 967-986, 1996.
- Bergstrom, R. W., Predictions of the Spectral Absorption and Extinction Coefficients of an Urban Air Pollution Model, *Atmospheric Environment*, 6, 247-258, 1972.
- Blumenthal, D. L., W. H. White, and T. B. Smith, Anatomy of a Los Angeles Smog Episode: Pollutant Transport in the Daytime Sea Breeze Regime, *Atmospheric Environment*, 12, 893-907, 1978.
- Bond, T. C., T. L. Anderson, and D. Campbell, Calibration and Intercomparison of Filter-Based Measurements of Visible Light Absorption by Aerosols, *Aerosol Science and Technology*, 30, 582-600, 1999.
- Castro, T., L. G. Ruizsuarez, J. C. Ruizsuarez, M. J. Molina, and M. Montero, Sensitivity Analysis of a Uv Radiation Transfer Model and Experimental Photolysis Rates of No₂ in the Atmosphere of Mexico City, *Atmospheric Environment*, 31, 609-620, 1997.
- Chow, J. C., J. G. Watson, E. M. Fujita, Z. Q. Lu, D. R. Lawson, and L. L. Ashbaugh, Temporal and Spatial Variations of Pm(2.5) And Pm(10) Aerosol in the Southern California Air-Quality Study, *Atmospheric Environment*, 28, 2061-2080, 1994.
- Chow, J. C., J. G. Watson, L. C. Pritchett, W. R. Pierson, C. A. Frazier, and R. G. Purcell, The Dri Thermal Optical Reflectance Carbon Analysis System - Description, Evaluation and Applications in United-States Air-Quality Studies, *Atmospheric Environment Part a-General Topics*, 27, 1185-1201, 1993.
- Demerjian, K. L., K. L. Schere, and J. T. Peterson, Theoretical Estimates of Actinic (Spherically Integrated) Flux and Photolytic Rate Constants of Atmospheric Species in the Lower Troposphere, *Adv. Environ. Sci. Technol.*, 10, 369-459, 1980.
- Dickerson, R. R., S. Kondragunta, G. Stenchikov, K. L. Civerolo, B. G. Doddridge, and B. N. Holben, The Impact of Aerosols on Solar Ultraviolet Radiation and Photochemical Smog, *Science*, 278, 827-830, 1997.
- Fuller, K. A., W. C. Malm, and S. M. Kreidenweis, Effects of Mixing on Extinction by Carbonaceous Particles, *Journal of Geophysical Research-Atmospheres*, 104, 15941-15954, 1999.
- Goodin, W. R., G. J. McRae, and J. H. Seinfeld, A Comparison of Interpolation Methods for Sparse Data: Application to Wind and Concentration Fields, *Journal of Applied Meteorology*, 18, 761-771, 1979.
- Harley, R. A., A. G. Russell, G. J. Mcrae, G. R. Cass, and J. H. Seinfeld, Photochemical Modeling of the Southern California Air-Quality Study, *Environmental Science & Technology*, 27, 378-388, 1993.
- Hoff, R. M., M. Harwood, A. Sheppard, F. Froude, J. B. Martin, and W. Strapp, Use of Airborne Lidar to Determine Aerosol Sources and Movement in the Lower Fraser Valley (Lfv), Bc, *Atmospheric Environment*, 31, 2123-2134, 1997.
- Jacobson, M. Z., Development and Application of a New Air Pollution Modeling System .3. Aerosol-Phase Simulations, *Atmospheric Environment*, 31, 587-608, 1997.
- Jacobson, M. Z., Studying the Effects of Aerosols on Vertical Photolysis Rate Coefficient and Temperature Profiles Over an Urban Airshed, *Journal of Geophysical Research-Atmospheres*, 103, 10593-10604, 1998.

- Kasten, F., Visibility in the Phase of Pre-condensation, *Tellus*, 21, 631-635, 1969.
- Lalas, D. P., D. N. Asimakopoulos, D. G. Deligiorgi, and C. G. Helmis, Sea-breeze Circulation and Photochemical Pollution in Athens, Greece, *Atmospheric Environment*, 17, 1621-1632, 1983.
- Lantz, K. O., R. E. Shetter, C. A. Cantrell, S. J. Flocke, J. G. Calvert, and S. Madronich, Theoretical, Actinometric, and Radiometric Determinations of the Photolysis Rate Coefficient of NO_2 During the Mauna Loa Observatory Photochemistry Experiment 2, *Journal of Geophysical Research-Atmospheres*, 101, 14613-14629, 1996.
- Larson, S. M., G. R. Cass, K. J. Hussey, and F. Luce, Verification of Image-Processing Based Visibility Models, *Environmental Science & Technology*, 22, 629-637, 1988.
- Li, S. M., A. M. Macdonald, J. W. Strapp, Y. N. Lee, and X. L. Zhou, Chemical and Physical Characterizations of Atmospheric Aerosols Over Southern California, *Journal of Geophysical Research-Atmospheres*, 102, 21341-21353, 1997.
- Liao, H., Y. L. Yung, and J. H. Seinfeld, Effects of Aerosols on Tropospheric Photolysis Rates in Clear and Cloudy Atmospheres, *Journal of Geophysical Research-Atmospheres*, 104, 23697-23707, 1999.
- Lu, R. and R. P. Turco, Air Pollutant Transport in a Coastal Environment .1. 2- Dimensional Simulations of Sea-Breeze and Mountain Effects, *Journal of the Atmospheric Sciences*, 51, 2285-2308, 1994.
- Lu, R. and R. P. Turco, Air Pollutant Transport in a Coastal Environment .2. 3- Dimensional Simulations Over Los-Angeles Basin, *Atmospheric Environment*, 29, 1499-1518, 1995.
- Lu, R., R. P. Turco, and M. Z. Jacobson, An Integrated Air Pollution Modeling System for Urban and Regional Scales .1. Structure and Performance, *Journal of Geophysical Research-Atmospheres*, 102, 6063-6079, 1997.
- Lurmann, F. W., A. S. Wexler, S. N. Pandis, S. Musarra, N. Kumar, and J. H. Seinfeld, Modelling Urban and Regional Aerosols .2. Application to California's South Coast Air Basin, *Atmospheric Environment*, 31, 2695-2715, 1997.
- Malicet, J., D. Daumont, J. Charbonnier, C. Parisse, A. Chakir, and J. Brion, Ozone Uv Spectroscopy .2. Absorption Cross-Sections and Temperature-Dependence, *Journal of Atmospheric Chemistry*, 21, 263-273, 1995.
- McNair, L. A., R. A. Harley, and A. G. Russell, Spatial Inhomogeneity in Pollutant Concentrations, and Their Implications for Air Quality Model Evaluation, *Atmospheric Environment*, 30, 4291-4301, 1996.
- Meng, Z., D. Dabdub, and J. H. Seinfeld, Chemical Coupling Between Atmospheric Ozone and Particulate Matter, *Science*, 277, 116-119, 1997.
- Meng, Z. Y., D. Dabdub, and J. H. Seinfeld, Size-Resolved and Chemically Resolved Model of Atmospheric Aerosol Dynamics, *Journal of Geophysical Research-Atmospheres*, 103, 3419-3435, 1998.
- Moelwyn-Hughes, E. A., Physical Chemistry, Pergamon, Tarrytown, NY, 1961.
- Neckel, H. and D. Labs, The Solar-Radiation Between 3300-Å and 12500-Å, *Solar Physics*, 90, 205-258, 1984.
- Pandis, S. N., R. A. Harley, G. R. Cass, and J. H. Seinfeld, Secondary Organic Aerosol Formation and Transport, *Atmospheric Environment Part a-General Topics*, 26, 2269-2282, 1992.

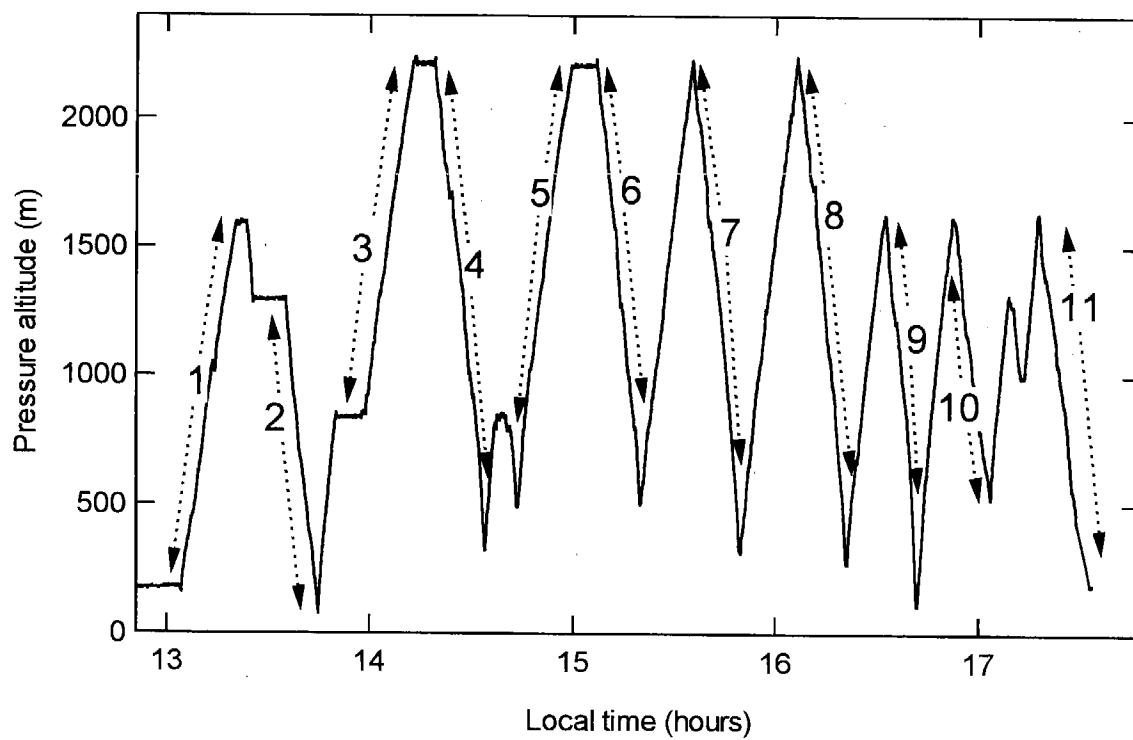
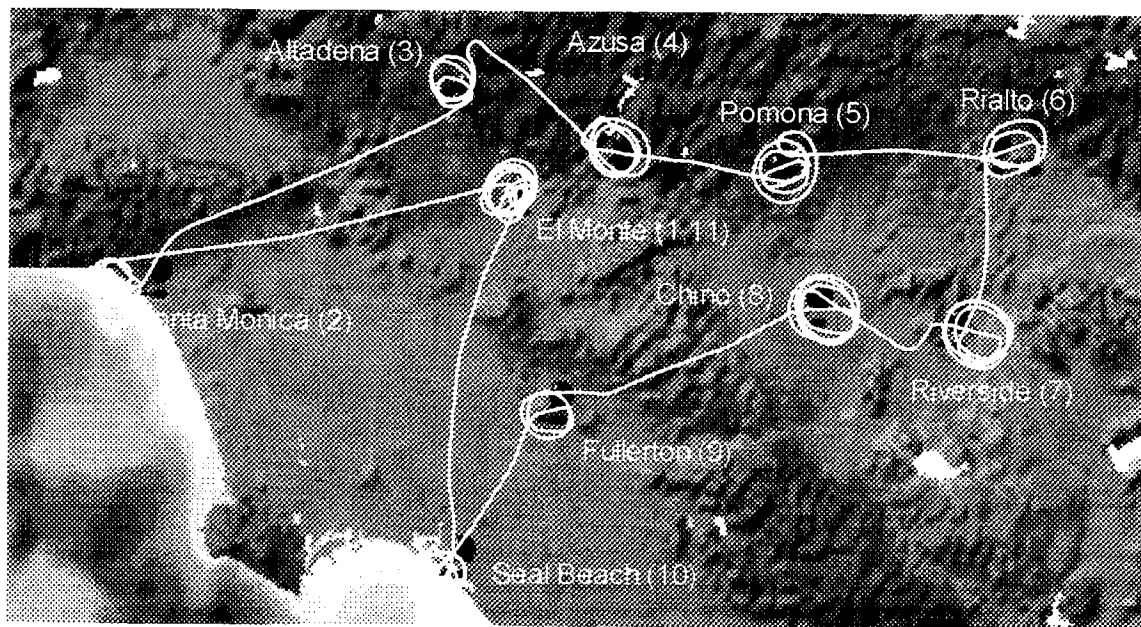
- Pandis, S. N., A. S. Wexler, and J. H. Seinfeld, Secondary Organic Aerosol Formation and Transport .2. Predicting the Ambient Secondary Organic Aerosol-Size Distribution, *Atmospheric Environment Part a-General Topics*, 27, 2403-2416, 1993.
- Patterson, E. M., Gillette D. A., and B. H. Stockton, Complex Index of Refraction Between 300 and 700 nm for Saharan Aerosols, *Journal of Geophysical Research*, 82, 3153-3160, 1977.
- Ruggaber, A., R. Dlugi, and T. Nakajima, Modeling Radiation Quantities and Photolysis Frequencies in the Troposphere, *Journal of Atmospheric Chemistry*, 18, 171-210, 1994.
- Saxena, P., L. M. Hildemann, P. H. McMurry, and J. H. Seinfeld, Organics Alter Hygroscopic Behavior of Atmospheric Particles, *Journal of Geophysical Research-Atmospheres*, 100, 18755-18770, 1995.
- Seinfeld, J. H. and S. N. Pandis, *Atmospheric Chemistry and Physics*, Wiley-Interscience, New York, 1998.
- Stamnes, K., S. C. Tsay, W. Wiscombe, and K. Jayaweera, Numerically Stable Algorithm for Discrete-Ordinate-Method Radiative-Transfer in Multiple-Scattering and Emitting Layered Media, *Applied Optics*, 27, 2502-2509, 1988.
- Tang, I. N., Chemical and Size Effects of Hygroscopic Aerosols on Light Scattering Coefficients, *Journal of Geophysical Research-Atmospheres*, 101, 19245-19250, 1996.
- Tang, I. N. and H. R. Munkelwitz, Water Activities, Densities, and Refractive-Indexes of Aqueous Sulfates and Sodium-Nitrate Droplets of Atmospheric Importance, *Journal of Geophysical Research-Atmospheres*, 99, 18801-18808, 1994.
- Tang, I. N., A. C. Tridico, and K. H. Fung, Thermodynamic and Optical Properties of Sea Salt Aerosols, *Journal of Geophysical Research-Atmospheres*, 102, 23269-23275, 1997.
- Tegen, I. and I. Fung, Modeling of Mineral Dust in the Atmosphere - Sources, Transport, and Optical-Thickness, *Journal of Geophysical Research-Atmospheres*, 99, 22897-22914, 1994.
- Wakamatsu, S., Y. Ogawa, K. Murano, K. Goi, and Y. Aburamoto, Aircraft Survey of the Secondary Photochemical Pollutants Covering the Tokyo Metropolitan Area, *Atmospheric Environment*, 17, 827-835, 1983.
- Wakimoto, R. M. and J. L. McElroy, Lidar Observation of Elevated Pollution Layers Over Los-Angeles, *Journal of Climate and Applied Meteorology*, 25, 1583-1599, 1986.
- White, W. H. Contribution to Light Extinction in Acid Deposition, State of Science and Technology. 90. Washington, D. C., Natl. Acid Precip. Assess. Program.
- World Meteorological Organization (WMO). Atmospheric Ozone. 85.

Appendix A: Flight details

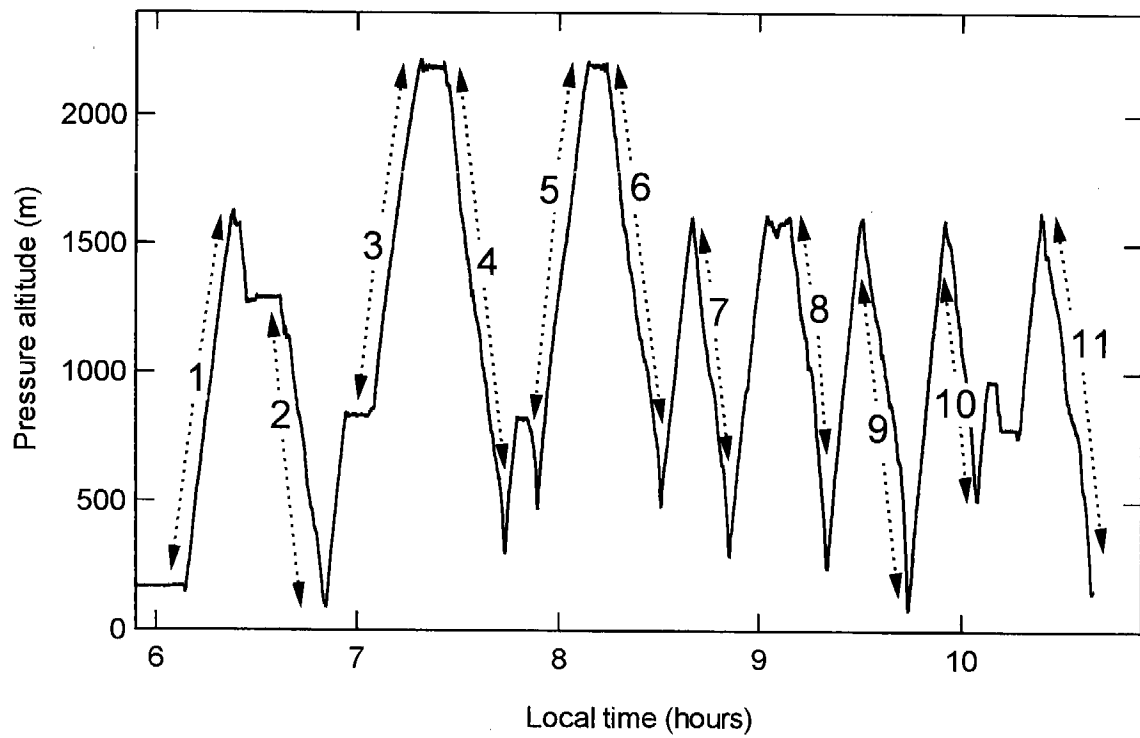
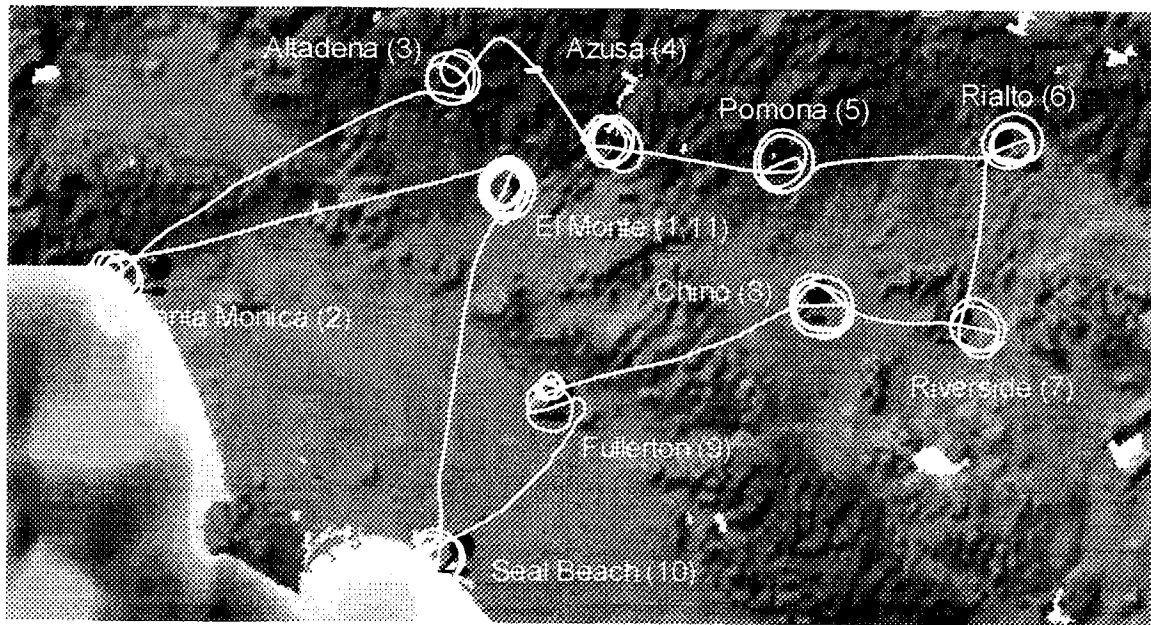
Flight # 1: 8/27/97 06:06 - 10:33



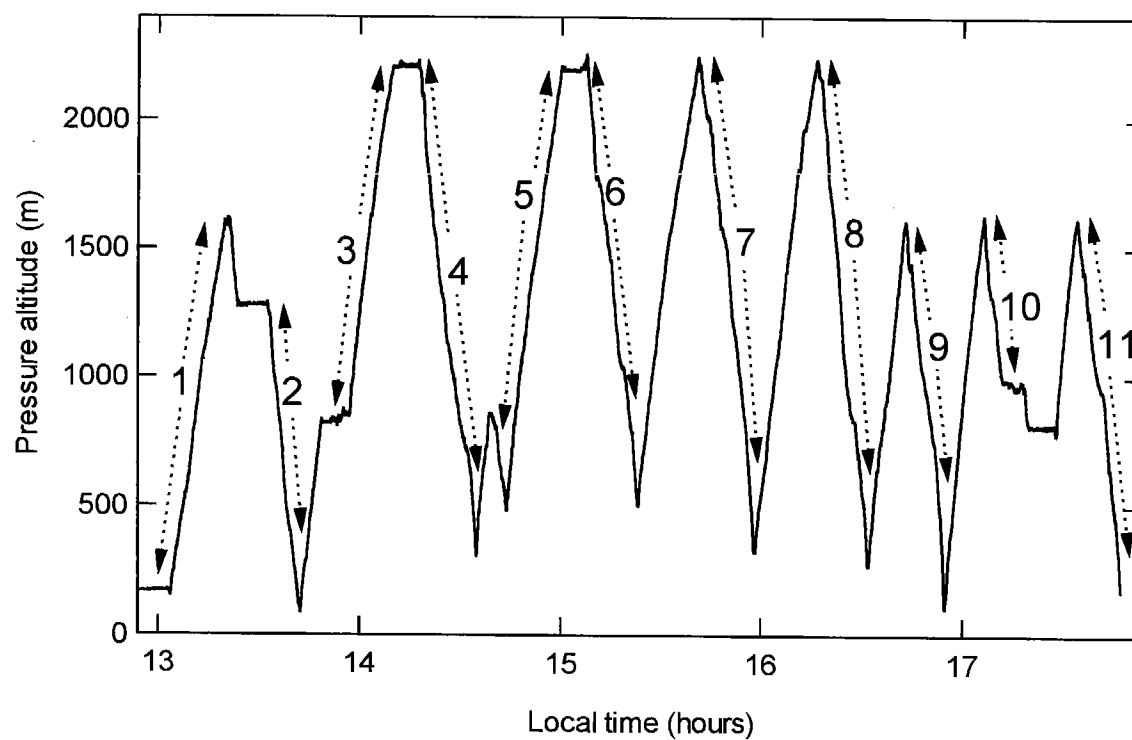
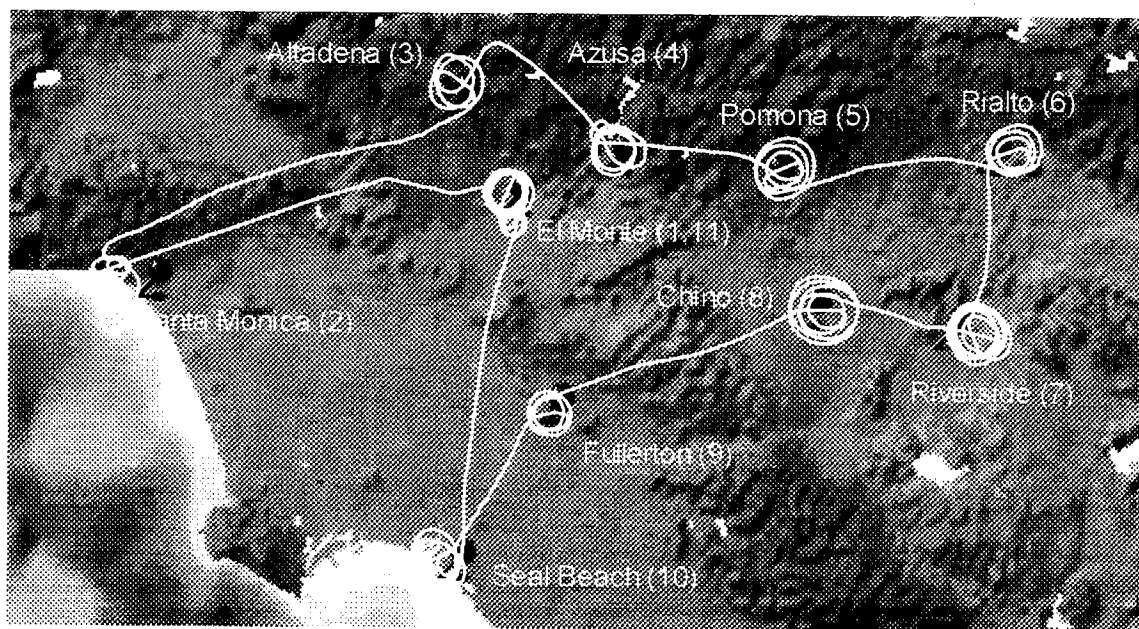
Flight # 2: 8/27/97 13:03 - 17:29



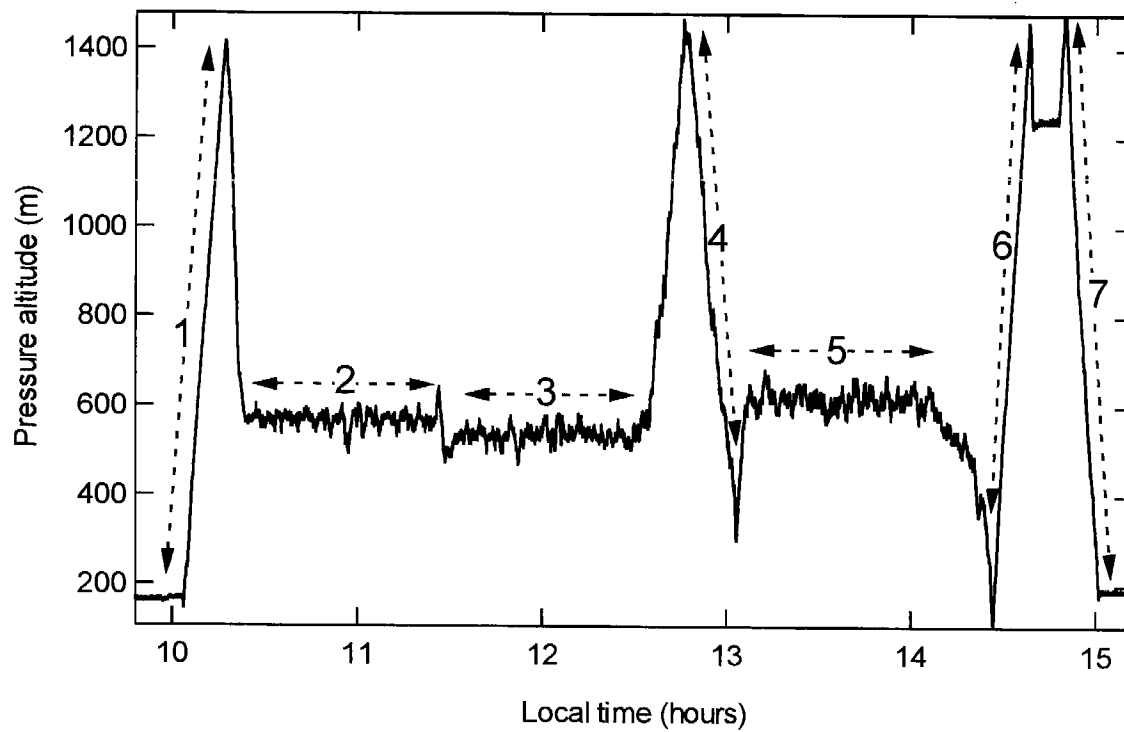
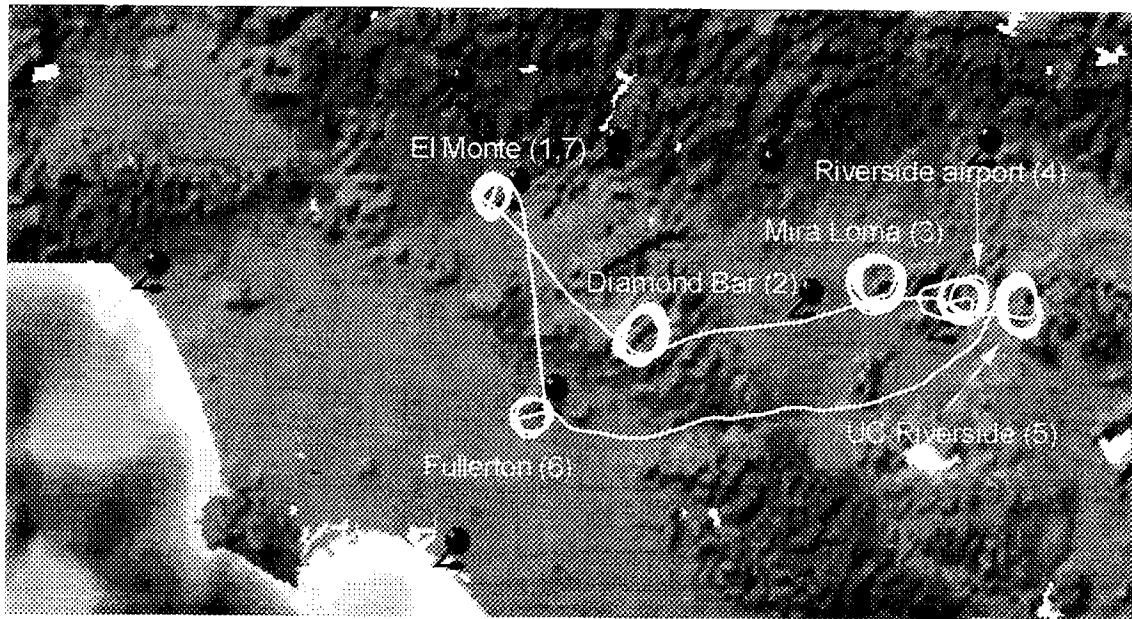
Flight # 3: 8/28/97 06:08 - 10:40



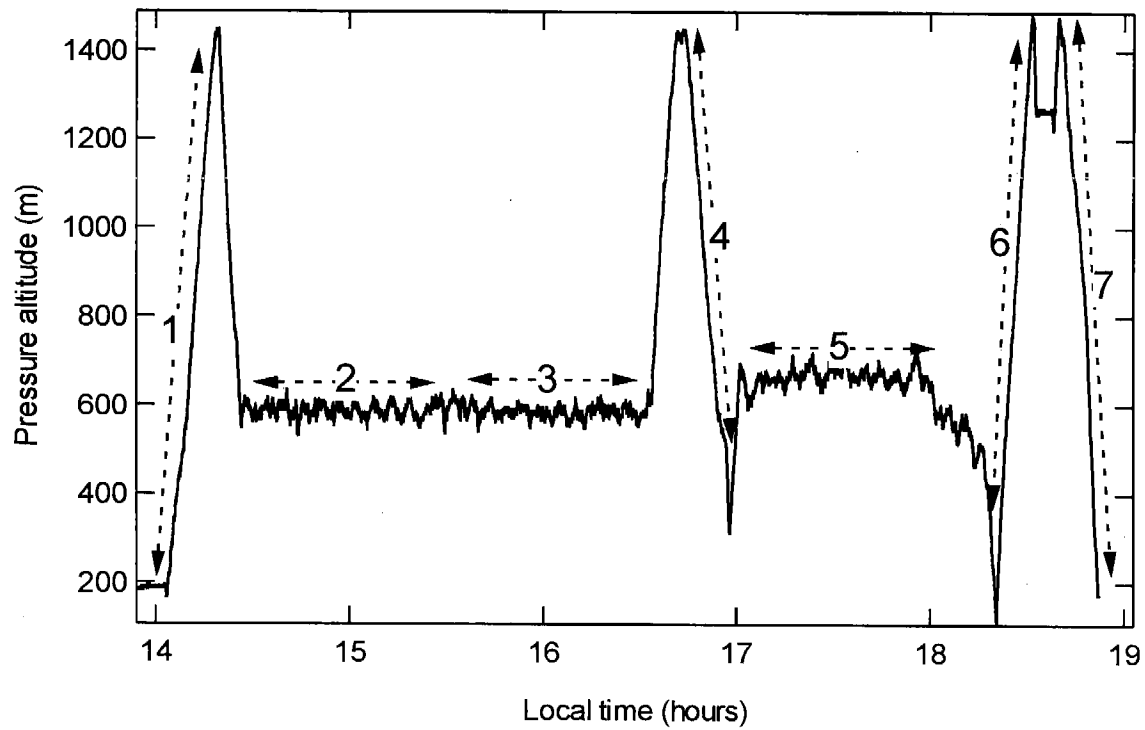
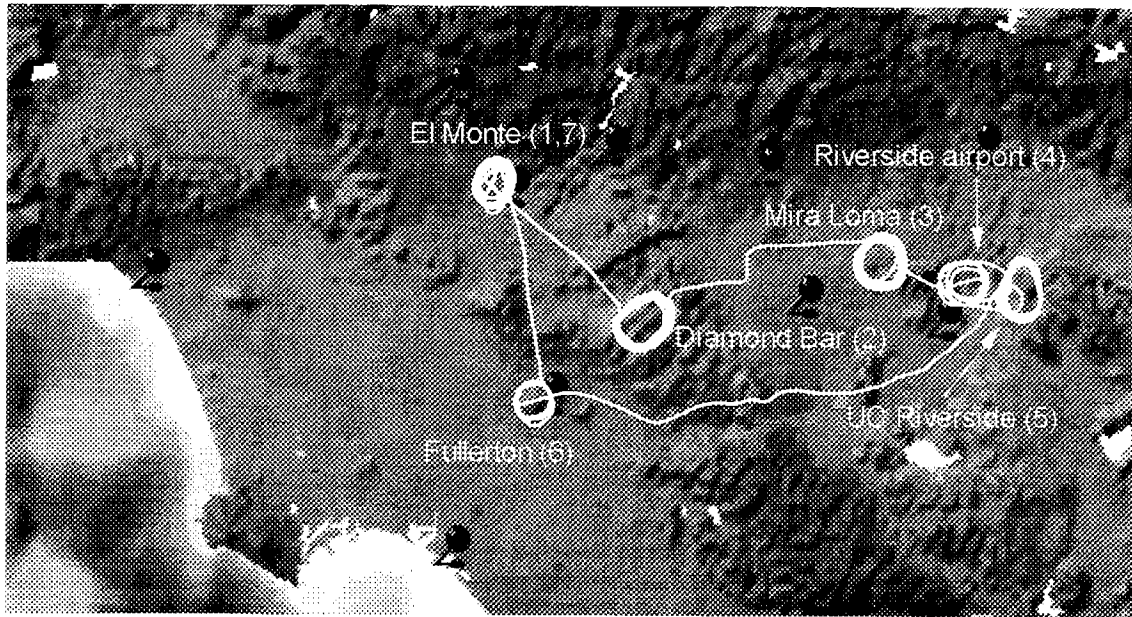
Flight # 4: 8/28/97 13:00 - 17:45



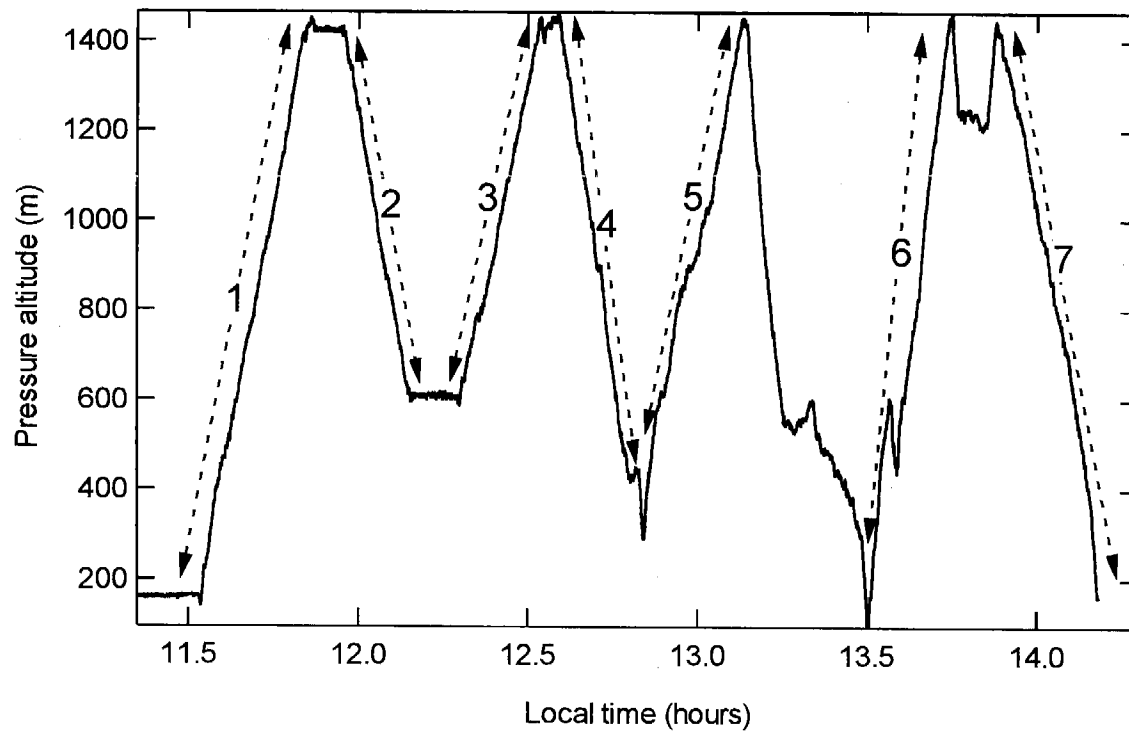
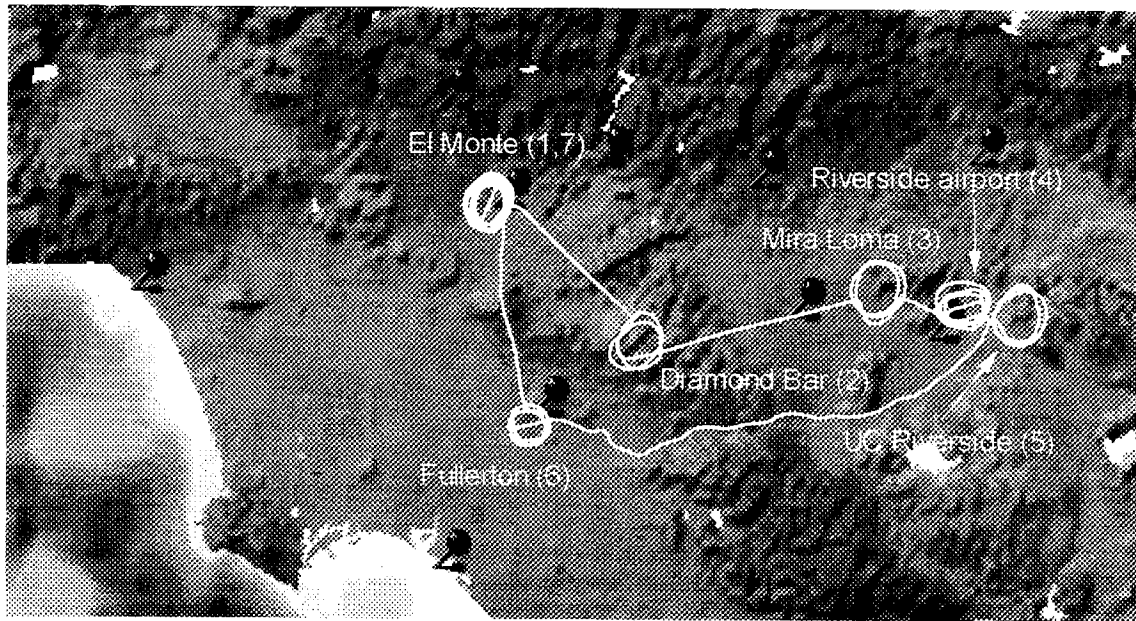
Flight # 5: 9/4/97 09:50 - 14:55



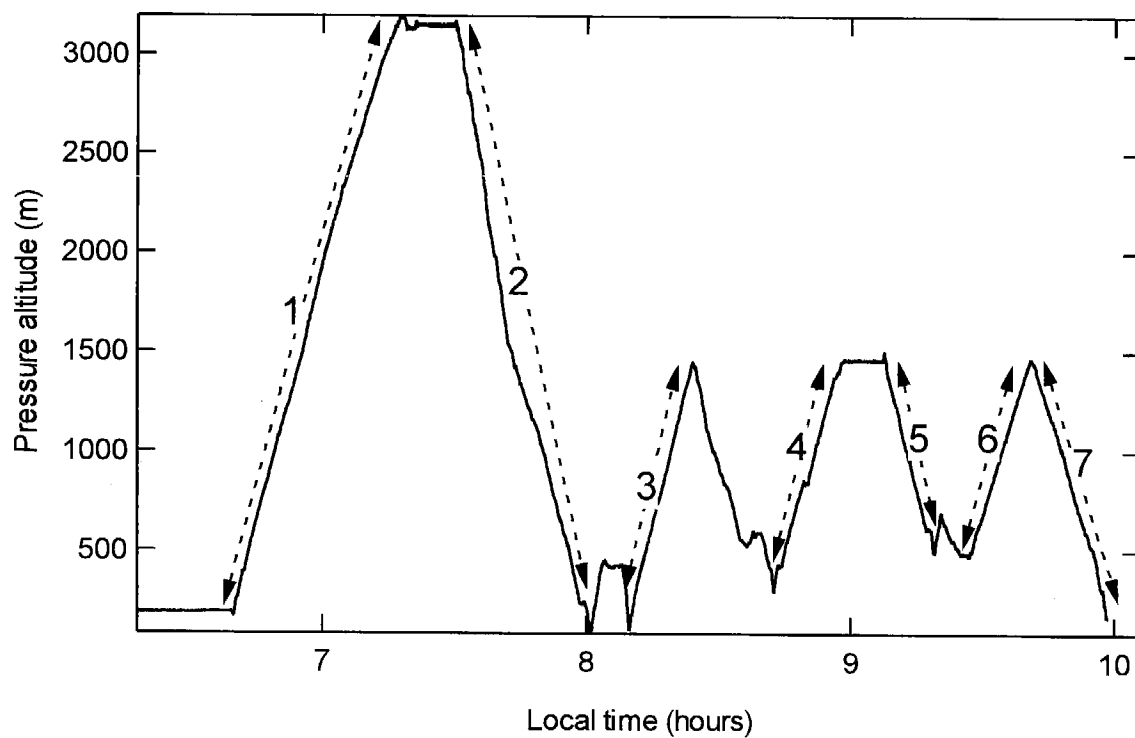
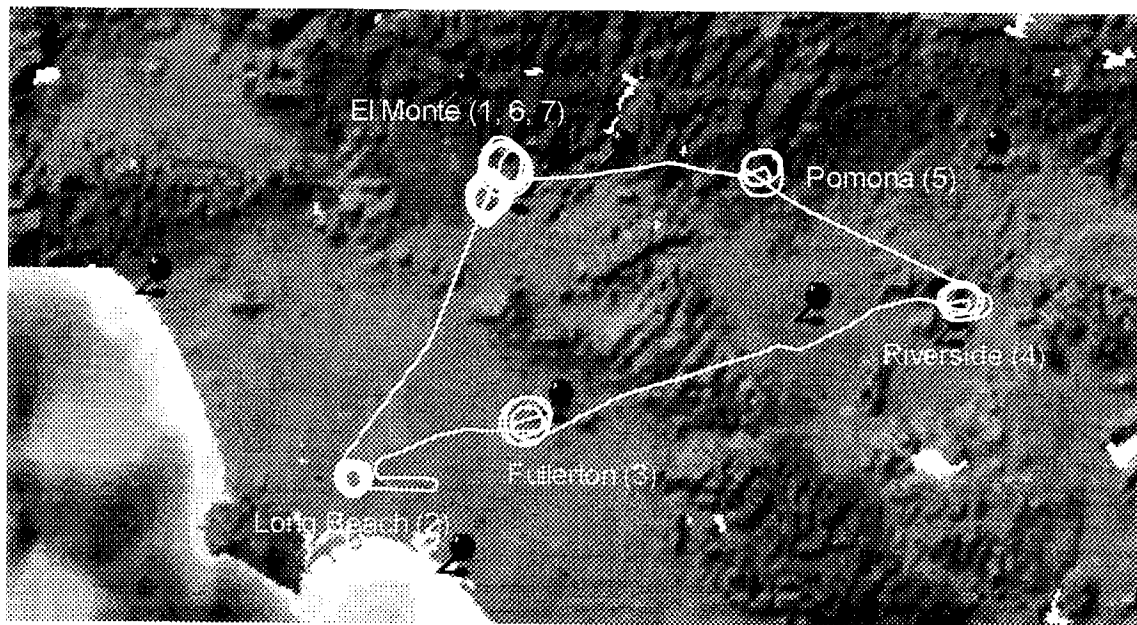
Flight # 6: 9/5/97 13:50 - 18:55



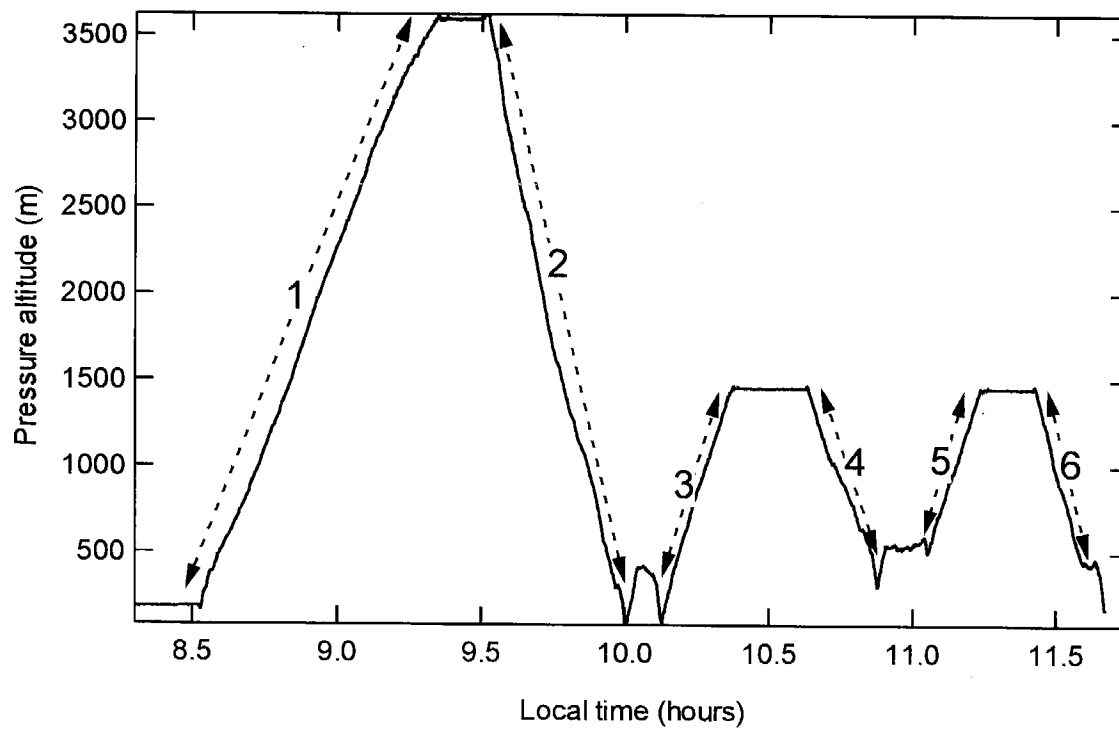
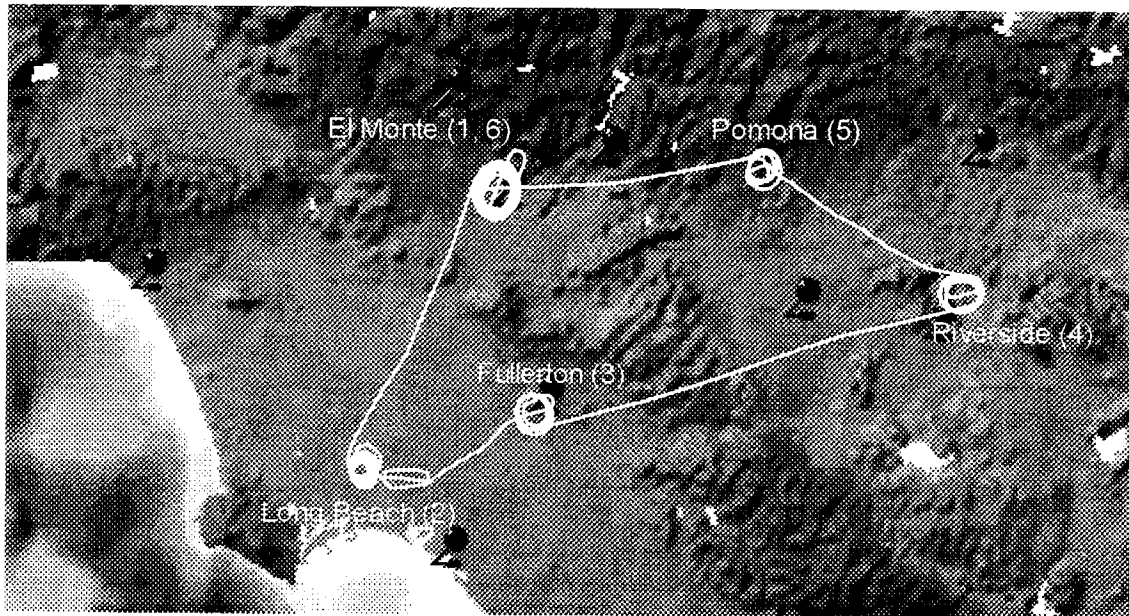
Flight # 7: 9/6/97 11:30 - 14:44



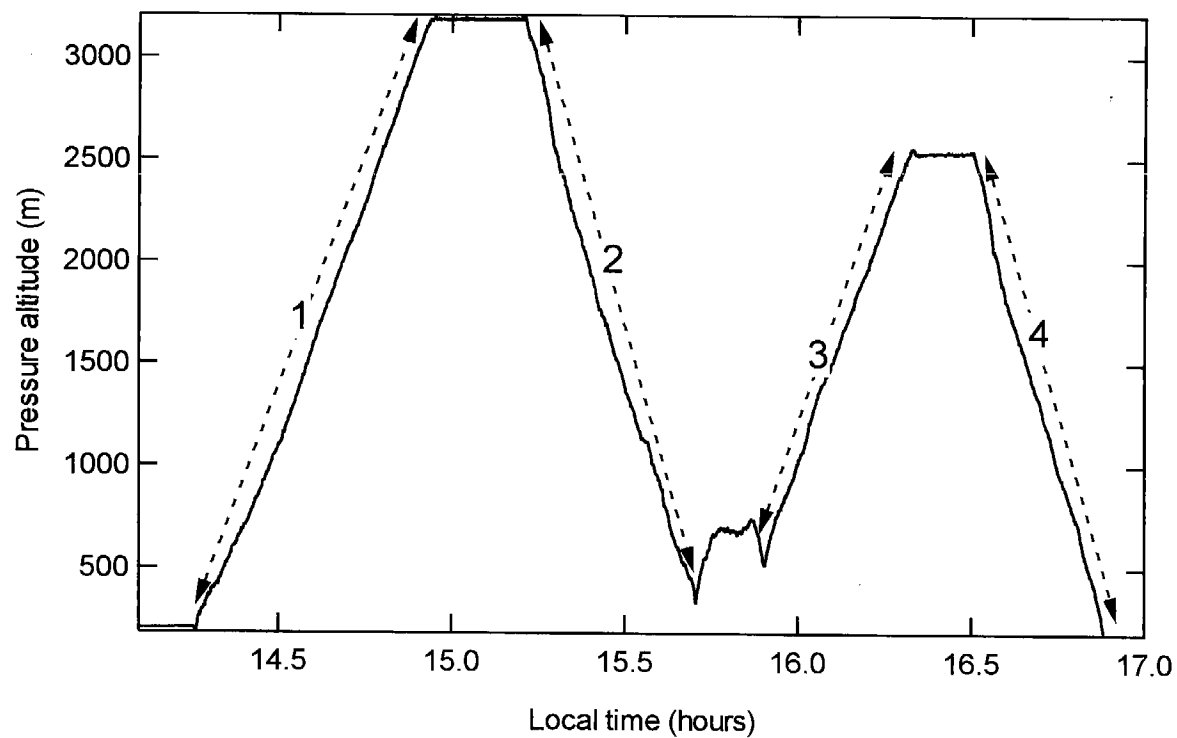
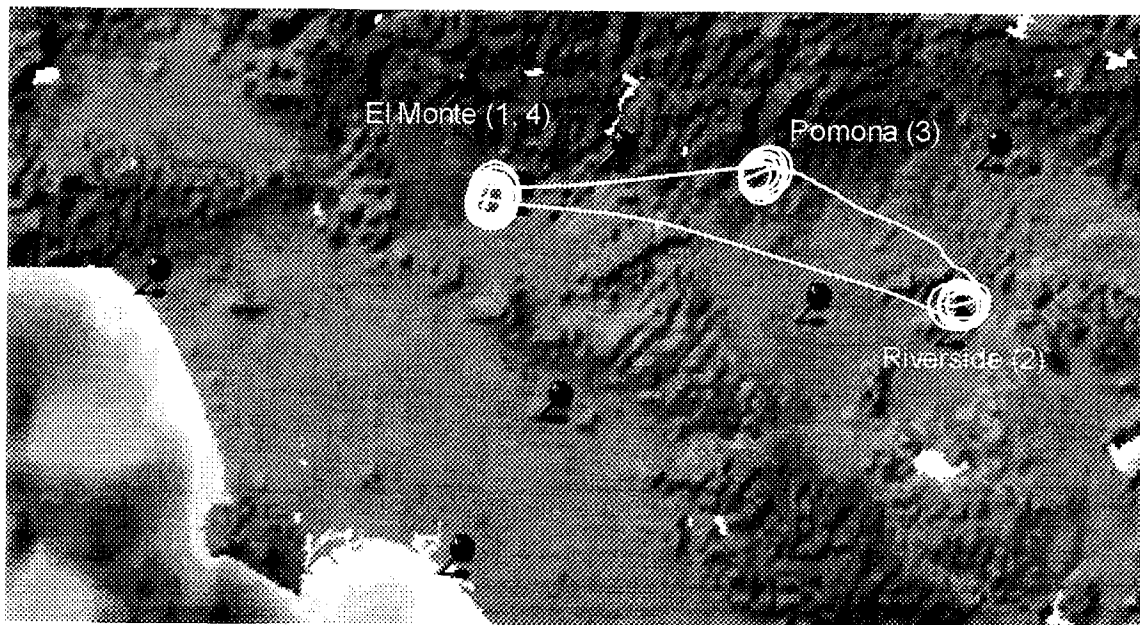
Flight # 8: 9/9/97 06:40 - 09:36



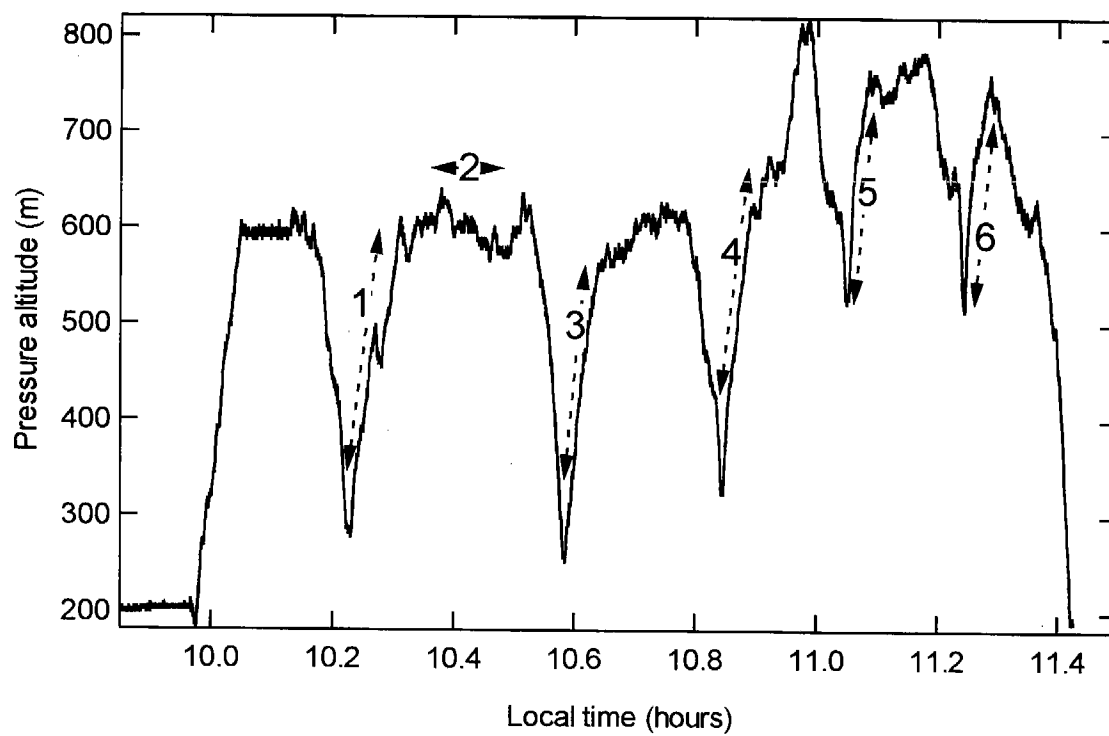
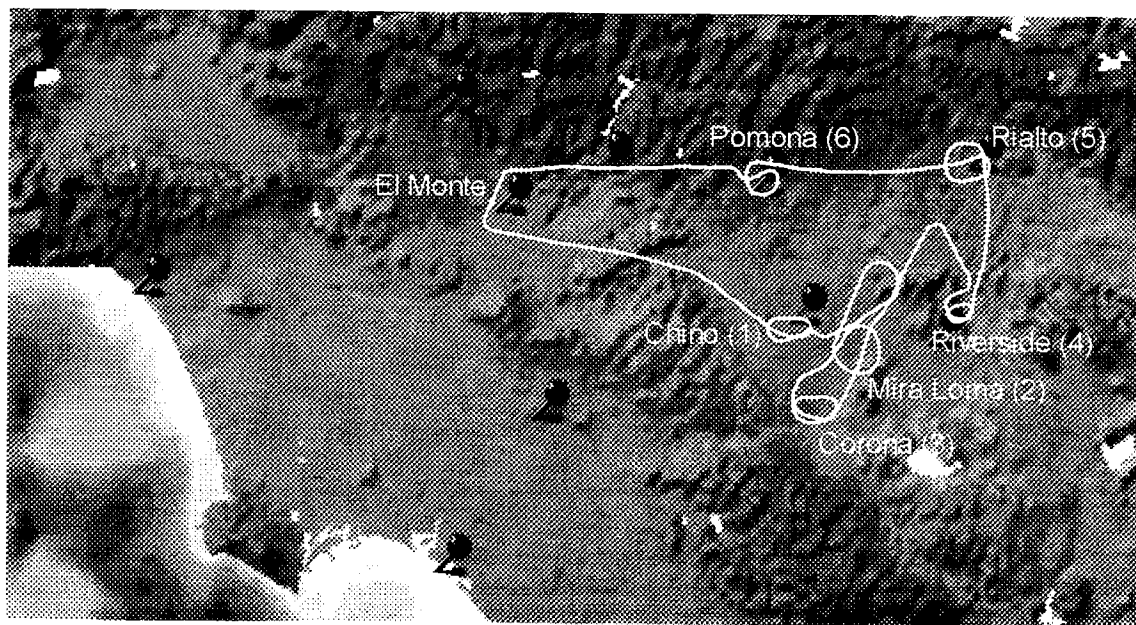
Flight # 9: 9/10/97 08:30 - 11:52



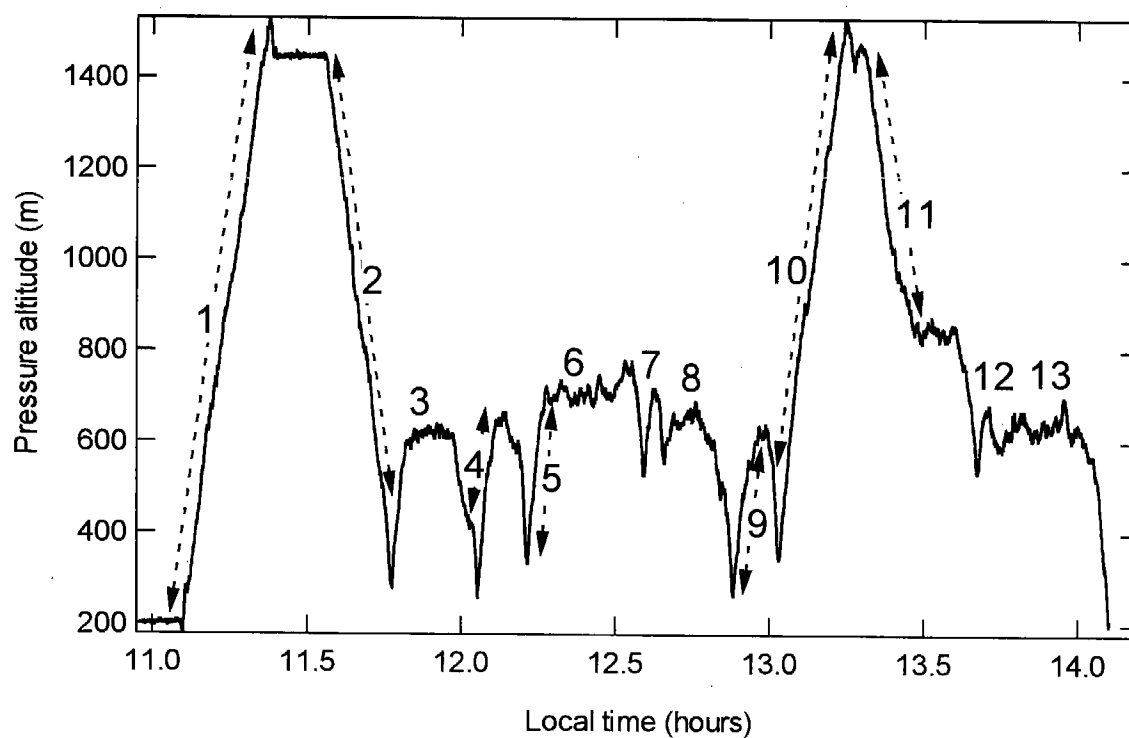
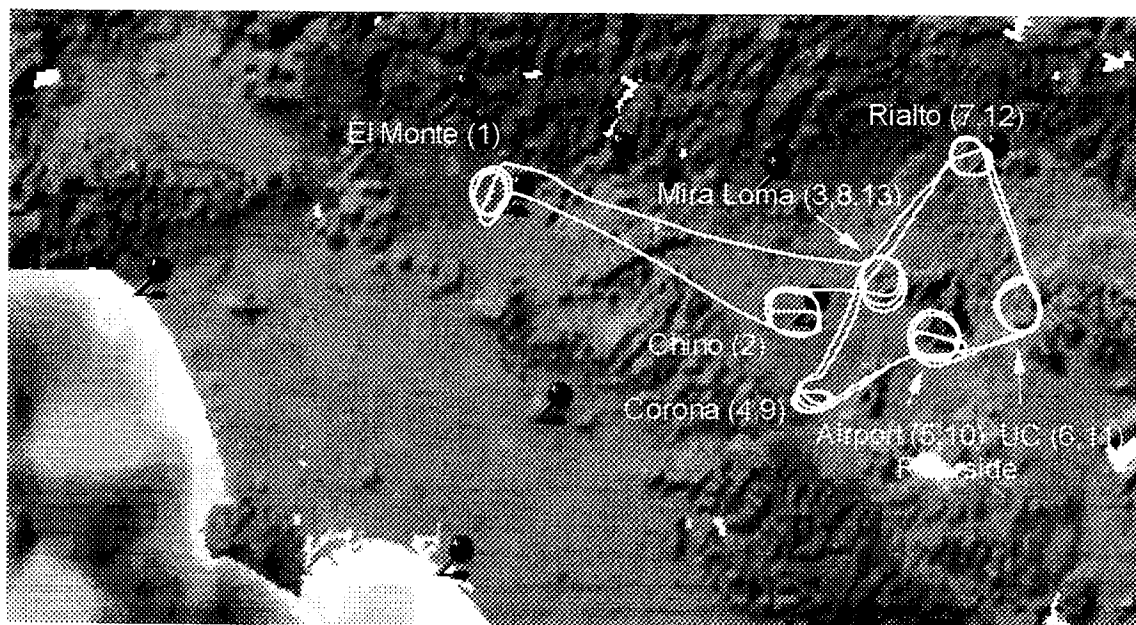
Flight # 10: 9/10/97 14:00 - 16:55



Flight # 11: 9/11/97 10:00 - 11:39



Flight # 12: 9/12/97 10:55 - 14:19



Appendix B: Filter data

Average filter flow rates and sampled volume

Flt	Leg	ID	Ambient flow Lpm	STP flow Lpm	Duration min	Ambient vol. m ³	STP vol. m ³
1	A1	LA1A1	24.21949	19.81	90	2.18	1.78
1	A2	LA1A2	23.13150	19.33	65	1.50	1.26
1	A3	LA1A3	24.20507	19.69	109	2.64	2.15
1	B1	LA1B1	24.40858	19.97	90	2.20	1.80
1	B2	LA1B2	24.19174	19.56	65	1.57	1.27
1	B3	LA1B3	24.68086	20.18	109	2.69	2.20
1	C1	LA1C1	24.43854	19.99	90	2.20	1.80
1	C2	LA1C2	24.20231	19.55	65	1.57	1.27
1	C3	LA1C3	24.33498	19.79	109	2.65	2.16
2	A1	LA2A1	23.04790	18.69	90	2.07	1.68
2	A2	LA2A2	23.15410	18.31	76	1.76	1.39
2	A3	LA2A3	23.41360	19.06	99	2.32	1.89
2	B1	LA2B1	24.35060	19.73	90	2.19	1.78
2	B2	LA2B2	23.97380	18.95	76	1.82	1.44
2	B3	LA2B3	23.97640	19.51	99	2.37	1.93
2	C1	LA2C1	23.16150	18.75	90	2.08	1.69
2	C2	LA2C2	24.08060	19.04	76	1.83	1.45
2	C3	LA2C3	24.32680	19.81	99	2.41	1.96
3	A1	LA3A1	23.82600	19.60	95	2.26	1.86
3	A2	LA3A2	24.04580	19.60	67	1.61	1.31
3	A3	LA3A3	24.20180	20.21	107	2.59	2.16
3	B1	LA3B1	24.31970	20.03	95	2.31	1.90
3	B2	LA3B2	24.23590	19.74	67	1.62	1.32
3	B3	LA3B3	24.10960	20.08	107	2.58	2.15
3	C1	LA3C1	23.14210	19.06	95	2.20	1.81
3	C2	LA3C2	25.02740	20.40	67	1.68	1.37
3	C3	LA3C3	23.96937	19.78	107	2.56	2.12
4	A1	LA4A1	23.02532	18.91	92	2.12	1.74
4	A2	LA4A2	23.06465	18.32	83	1.91	1.52
4	A3	LA4A3	23.30601	19.16	109	2.54	2.09
4	B1	LA4B1	23.82228	19.56	92	2.19	1.80
4	B2	LA4B2	22.38490	17.78	83	1.86	1.48
4	B3	LA4B3	22.66191	18.63	109	2.47	2.03
4	C1	LA4C1	22.65846	18.61	92	2.08	1.71
4	C2	LA4C2	22.85909	18.15	83	1.90	1.51
4	C3	LA4C3	22.89210	18.81	109	2.50	2.05
5	A1	LA5A1	22.97880	19.73	61	1.40	1.20
5	A2	LA5A2	22.93490	19.34	91	2.09	1.76

Average filter flow rates and sampled volume (continued)

Flt	Leg	ID	Ambient flow Lpm	STP flow Lpm	Duration min	Ambient vol. m ³	STP vol. m ³
5	A3	LA5A3	22.53550	18.97	60	1.35	1.14
5	B1	LA5B1	23.58580	20.25	61	1.44	1.24
5	B2	LA5B2	23.89970	20.16	91	2.17	1.83
5	B3	LA5B3	23.04110	19.39	60	1.38	1.16
5	C1	LA5C1	23.62990	20.28	61	1.44	1.24
5	C2	LA5C2	23.30490	19.66	91	2.12	1.79
5	C3	LA5C3	23.08960	19.39	60	1.39	1.16
6	A1	LA6A1	22.56030	19.37	60	1.35	1.16
6	A2	LA6A2	22.18440	18.90	56	1.24	1.06
6	A3	LA6A3	22.49490	19.06	62	1.39	1.18
6	B1	LA6B1	23.60930	20.23	60	1.42	1.21
6	B2	LA6B2	23.06680	19.65	56	1.29	1.10
6	B3	LA6B3	23.22160	19.67	62	1.44	1.22
6	C1	LA6C1	22.30950	19.14	60	1.34	1.15
6	C2	LA6C2	22.93820	19.54	56	1.28	1.09
6	C3	LA6C3	23.17020	19.63	62	1.44	1.22
7	A1	LA7A1	24.00000	19.00	60	1.44	1.14
7	A2	LA7A2	22.92223	18.93	53	1.21	1.00
7	A3	LA7A3	23.03901	19.40	59	1.36	1.14
7	B1	LA7B1	24.00000	19.00	60	1.44	1.14
7	B2	LA7B2	23.74262	19.60	53	1.26	1.04
7	B3	LA7B3	23.38712	19.70	59	1.38	1.16
7	C1	LA7C1	24.00000	19.00	60	1.44	1.14
7	C2	LA7C2	23.50868	19.40	53	1.25	1.03
7	C3	LA7C3	23.77928	20.03	59	1.40	1.18
8	A1	LA8A1	24.00000	19.00	60	1.44	1.14
8	A2	LA8A2	24.00000	19.00	60	1.44	1.14
8	A3	LA8A3	24.00000	19.00	60	1.44	1.14
8	B1	LA8B1	24.00000	19.00	60	1.44	1.14
8	B2	LA8B2	24.00000	19.00	60	1.44	1.14
8	B3	LA8B3	24.00000	19.00	60	1.44	1.14
8	C1	LA8C1	24.00000	19.00	60	1.44	1.14
8	C2	LA8C2	24.00000	19.00	60	1.44	1.14
8	C3	LA8C3	24.00000	19.00	60	1.44	1.14

Filter blank results

Gravimetric Mass Blanks

Filt ID	Date	Leg	Filter Type	ID	Grav. Mass Blank (µg/filter)
71	9/6/97	Leg A	Teflon	T37	-6.0±5.4
81	9/7/97	"	"	T43	4.0±5.4
82	9/7/97	"	"	T44	4.0±5.4
83	9/7/97	"	"	T45	4.0±5.4
71	9/6/97	Leg C	Teflon	T40	0.0±5.4
81	9/7/97	"	"	T46	5.0±5.4
82	9/7/97	"	"	T47	-5.0±5.4
83	9/7/97	"	"	T48	0.0±5.4
Average Teflon Filter Mass Blank (µg/filter)					0.8±4.3

Carbon Blanks

Filt ID	Date	Leg	Filter Type	ID	Organic Carbon	Elemental Carbon
71	9/6/97	Leg B	Quartz	QA37	1.2±0.9	0.1±0.2
81	9/7/97	"	"	QA43	1.2±0.9	0.0±0.2
82	9/7/97	"	"	QA45	1.7±0.9	0.0±0.2
83	9/7/97	"	"	QA47	1.6±0.9	1.0±0.3
71	9/6/97	"	"	QB38	0.8±0.9	0.0±0.2
81	9/7/97	"	"	QB44	1.1±0.9	0.0±0.2
82	9/7/97	"	"	QB46	2.7±1.0	1.1±0.3
83	9/7/97	"	"	QB48	1.4±0.9	0.0±0.2
Average Quartz Filter Carbon Blanks (µg/filter)					1.5±0.6	0.3±0.5

Teflon Filter Ion Blanks

Filt ID	Date	Leg	Filter Type	ID	Nitrate	Sulfate	Ammonium
71	9/6/97	Leg C	Teflon	T40	0.0±0.2	0.1±0.2	0.0±0.3
81	9/7/97	"	"	T46	0.0±0.2	0.1±0.2	0.2±0.3
82	9/7/97	"	"	T47	0.0±0.2	0.1±0.2	0.2±0.3
83	9/7/97	"	"	T48	0.1±0.2	0.1±0.2	0.2±0.3
Average Teflon Filter Ion Blanks (µg/filter)					0.0±0.1	0.1±0.0	0.1±0.1

Nylon Filter Blank

Filt ID	Date	Leg	Filter Type	ID	Nitrate
71	9/6/97	Leg C	Nylon	N19	2.0±0.3
81	9/7/97	"	"	N22	1.2±0.3
82	9/7/97	"	"	N23	1.0±0.3
83	9/7/97	"	"	N24	1.1±0.3
Average Nylon Filter Nitrate Blank (µg/filter)					1.3±0.5

Unadjusted gravimetric and species mass data ($\mu\text{g m}^{-3}$)

Flt	Leg	MassA	MassC	NO ₃ ⁻ (Tef)	NO ₃ ⁻ (Nyl)	NH ₄ ⁺ (Tef)	SO ₄ ²⁻ (Tef)	OC (front)	OC (back)	EC (front)	EC (back)	Na ⁺	Mg ²⁺	Al ³⁺	Si ⁴⁺	K ⁺	Fe ³⁺	Ni ²⁺	Cu ²⁺	Zn ²⁺
1	1	5.7	5.2	0.3	1.5	0.3	0.9	3.4	1.	0.1	-0.1	0.12	0.016	0.016	0.17	0.15	2.17	0.024	0.046	0.079
1	2	4.2	10.4	0.4	3.6	0.4	1.1	4.4	1.	0.3	-0.2	0.14	0.015	0.008	0.23	0.18	0.75	0.012	0.007	0.019
1	3	4.7	5.0	0.3	2.0	0.2	0.8	2.8	0.	0.3	-0.1	0.12	0.017	0.010	0.16	0.10	0.29	0.011	0.080	0.052
2	1	3.1	4.5	0.4	2.2	0.3	0.9	3.0	0.	0.5	-0.1	0.06	0.001	0.004	0.17	0.15	0.02	0.000	0.015	0.012
2	2	7.6	3.5	0.4	1.4	0.4	1.1	3.6	0.	0.6	0.1	0.17	0.018	0.016	0.25	0.18	0.13	0.004	0.002	0.008
2	3	5.3	6.8	0.3	1.2	0.3	0.9	1.7	0.	0.1	-0.1	0.05	0.001	0.001	0.17	0.13	0.02	0.005	0.009	0.007
3	1	5.0	4.7	0.5	1.4	0.3	0.9	2.0	0.	0.1	0.1	0.07	0.003	0.003	0.17	0.12	0.02	-0.001	0.001	0.003
3	2	10.2	9.2	0.4	5.3	0.4	1.3	1.7	0.	-0.1	-0.2	0.05	0.016	0.017	2.07	0.02	0.85	0.010	0.002	0.011
3	3	9.0	8.7	0.4	4.6	0.5	1.2	2.7	0.	0.4	-0.1	0.08	0.012	0.007	1.31	0.03	0.04	0.005	0.001	0.006
4	1	4.4	8.3	0.6	5.0	0.5	1.7	3.3	1.	0.6	0.0	0.08	0.013	0.010	1.62	0.04	0.24	0.227	0.038	0.025
4	2	11.2	13.4	0.5	4.9	0.5	1.5	2.6	-0.	0.9	-0.1	0.12	0.026	0.014	1.78	0.06	0.11	0.014	0.003	0.009
4	3	5.7	7.8	0.4	3.3	0.5	1.6	2.2	-0.	0.3	-0.1	0.03	0.000	0.001	0.14	0.07	0.01	-0.001	0.000	0.002
5	1	28.1	16.2	0.7	2.6	0.9	2.9	5.7	2.	3.4	-0.2	0.38	0.072	0.053	0.27	0.32	0.22	0.388	0.045	0.051
5	2	15.0	12.9	0.2	3.7	1.3	3.8	3.5	0.	0.7	0.0	0.05	0.003	0.006	0.15	0.15	0.03	0.001	0.001	0.012
5	3	14.3	3.2	0.2	0.5	1.5	4.4	4.9	0.	0.3	-0.2	0.06	-0.001	0.002	0.25	0.17	0.02	0.001	0.003	0.003
6	1	29.8	24.9	2.1	7.4	2.0	6.5	7.1	0.	1.8	-0.2	1.36	0.191	0.170	0.39	0.34	0.23	0.042	0.115	0.087
6	2	22.0	12.0	1.2	13.1	1.6	4.9	5.1	0.	1.5	-0.2	0.45	0.064	0.027	0.35	0.26	0.08	0.012	0.005	0.011
6	3	20.3	17.0	1.3	6.0	1.2	4.2	4.3	0.	1.0	-0.1	0.09	0.004	0.002	0.22	0.18	0.02	-0.002	0.001	0.002
7	2	9.4	18.8	0.6	19.6	0.7	2.5	3.8	0.	0.7	-0.1	0.12	0.015	0.015	0.25	0.18	0.05	0.007	0.007	0.006
7	3	19.4	22.4	0.8	9.0	1.1	4.4	6.4	-0.	1.0	-0.2	0.21	0.032	0.028	0.26	0.22	0.09	0.006	0.009	0.011
Avg		11.7	10.7	0.6	4.9	0.7	2.4	3.7	0.	0.7	-0.1	0.19	0.026	0.021	0.52	0.15	0.27	0.038	0.020	0.021